Numerical simulation of acoustic emission in brittle rocks by two-dimensional finite-discrete element analysis

A. Lisjak,[1] Q. Liu,[2] Q. Zhao,[1] O. K. Mahabadi[1] and G. Grasselli[1]

[1]*Department of Civil Engineering, University of Toronto,* 35 *St George Street, Toronto, Ontario* M5S 1A4, *Canada. E-mail: andrea.lisjak@utoronto.ca*
[2]*Department of Physics, University of Toronto,* 60 *St George Street, Toronto, Ontario* M5S 1A7, *Canada*

SUMMARY

Stress waves, known as acoustic emissions (AEs), are released by localized inelastic deformation events during the progressive failure of brittle rocks. Although several numerical models have been developed to simulate the deformation and damage processes of rocks, such as non-linear stress–strain behaviour and localization of failure, only a limited number have been capable of providing quantitative information regarding the associated seismicity. Moreover, the majority of these studies have adopted a pseudo-static approach based on elastic strain energy dissipation that completely disregards elastodynamic effects. This paper describes a new AE modelling technique based on the combined finite-discrete element method (FEM/DEM), a numerical tool that simulates material failure by explicitly considering fracture nucleation and propagation in the modelling domain. Given the explicit time integration scheme of the solver, stress wave propagation and the effect of radiated seismic energy can be directly captured. Quasi-dynamic seismic information is extracted from a FEM/DEM model with a newly developed algorithm based on the monitoring of internal variables (e.g. relative displacements and kinetic energy) in proximity to propagating cracks. The AE of a wing crack propagation model based on this algorithm are cross-analysed by traveltime inversion and energy estimation from seismic recordings. Results indicate a good correlation of AE initiation times and locations, and scaling of energies, independently calculated with the two methods. Finally, the modelling technique is validated by simulating a laboratory compression test on a granite sample. The micromechanical parameters of the heterogeneous model are first calibrated to reproduce the macroscopic stress–strain response measured during standard laboratory tests. Subsequently, AE frequency–magnitude statistics, spatial clustering of source locations and the evolution of AE rate are investigated. The distribution of event magnitude tends to decay as power law while the spatial distribution of sources exhibits a fractal character, in agreement with experimental observations. Moreover, the model can capture the decrease of seismic *b* value associated with the macrorupture of the rock sample and the transition of AE spatial distribution from diffuse, in the pre-peak stage, to strongly localized at the peak and post-peak stages, as reported in a number of published laboratory studies. In future studies, the validated FEM/DEM-AE modelling technique will be used to obtain further insights into the micromechanics of rock failure with potential applications ranging from laboratory-scale microcracking to engineering-scale processes (e.g. excavations within mines, tunnels and caverns, petroleum and geothermal reservoirs) to tectonic earthquakes triggering.

Key words: Numerical solutions; Geomechanics; Fracture and flow; Mechanics, theory, and modelling.

GJI Seismology

1 INTRODUCTION

Acoustic emissions (AEs) are broadly defined as high-frequency transient elastic waves generated by a sudden release of stored strain energy within a material (Lockner 1993). In brittle rocks,

AEs are triggered by localized inelastic deformation events, such as microcracking, pore collapsing and grain boundary slip, that characterize the material deformation and damage process.

In laboratory studies, AE recording has been used in passive geophysical monitoring to investigate the fracturing behaviour of brittle

rocks. Unlike traditional integral rock damage indicators, such as non-linear deformation and variation of elastic wave propagation properties, the AE method offers the advantage of detecting individual fracture events. Consequently, AE source location has been employed to experimentally observe the nucleation and growth of cracks and their eventual coalescence into a macroscopic fault (e.g. Lockner *et al.* 1991; Thompson *et al.* 2006; Benson *et al.* 2008). Using the variation of AE properties which occurs in response to the damage evolution, the staged character of the brittle fracturing and the associated characteristic stress threshold values have been analysed (Eberhardt *et al.* 1997). Furthermore, the Kaiser effect, the mechanism by which AEs are only detected during the first loading to a certain stress state under compression, has been used to assess the amount of damage developed in rocks (e.g. Holcomb *et al.* 1990). It has also been demonstrated that the seismogenic (i.e. brittle) failure is a self-similar and scale-invariant process over a dimension range that spans several orders of magnitude, from grain-scale cracking to mining-induced seismicity and tectonic earthquakes (Scholz 1968a; Hanks 1992). Therefore, the acoustic activity of rock recorded in the laboratory has been considered a small-scale equivalent system for the seismicity of rock masses or in the Earth's crust.

In the field, AE monitoring was historically introduced as a mine design and rockburst prediction tool (Obert & Duvall 1957). Subsequently, the method has been employed to characterize the evolution of the damaged zone around underground excavations (e.g. Young & Maxwell 1992; Falls & Young 1998; Pettitt *et al.* 2002), and, in petroleum and geothermal engineering, to study the fracture zone induced by fluid injection during hydraulic fracturing (e.g. Pearson 1981; Majer & Doe 1986; House 1987).

A great deal of research has focused on developing and validating numerical models that could capture the progressive mechanical breakdown of rocks (see Yuan & Harrison 2006). However, only a limited number have been capable of providing quantitative output relative to the associated acoustic activity. Moreover, the majority of these studies have been based on a static approach that disregards the radiated seismic energy and the elastic wave propagation, as further explained in Section 2. According to Hazzard & Young (2002), two main reasons can be identified for modelling AE in rocks. First, the ability to extract and quantify seismic information from the models, together with the simulated stress–strain behaviour and damage observations, can provide an additional tool to validate the modelling methodology and increase the confidence in the simulation results. Secondly, a successfully validated AE model can be used to investigate the relationships between simulated seismicity, damage and deformation characteristics, and model properties.

In this study, an innovative numerical approach, based on the combined finite-discrete element method (FEM/DEM) (Munjiza 2004; Mahabadi *et al.* 2012a), is proposed to simulate AE associated with the brittle failure of rock. It is shown that the seismic information, including AE initiation time, location and energy, obtained from the analysis of FEM/DEM synthetic seismograms can be related to the information extracted by monitoring the motions of AE sources within the model. The 2-D modelling technique is validated by simulating the acoustic activity of a granite sample under uniaxial compressive load.

The paper is organized as follows. In Section 2, the major studies on AE simulation are briefly reviewed. In particular, differences between material representation types (e.g. 'continuum' versus 'discontinuum') and AE modelling approaches (i.e. static versus dynamic) are highlighted. In Section 3, the fundamental principles of FEM/DEM are illustrated with special emphasis on the assumptions

inherent in the material failure modelling technique. In Section 4, the simulation of AE is discussed within the context of FEM/DEM. A new algorithm, developed to extract seismic information by internally monitoring AE sources, is presented (Section 4.2). The AE of a wing crack propagation model based on this algorithm are cross-analysed by traveltime inversion and energy estimation from seismic recordings (Section 4.3). Finally, in Section 5, the results of a compression test simulation on a heterogeneous rock are presented. The simulated acoustic activity is first analysed in relation to the macroscopic stress–strain behaviour of the sample. Subsequently, the AE frequency–magnitude statistics, clustering behaviour and rate evolution are discussed with reference to published experimental results.

2 RELATED STUDIES ON AE SIMULATION

Three main modelling methodologies have been adopted to simulate the acoustic activity associated with the failure process of brittle and quasi-brittle materials: (i) continuum damage models, (ii) particle-based DEM models and (iii) lattice models. Moreover, a fourth class of models can be identified, which focuses exclusively on the emission of acoustic waves from a single crack propagating in an elastic medium.

In continuum damage models, the effect of fracturing on the material mechanical behaviour is smeared over the material volume that contains the potential crack by degrading the corresponding material properties (e.g. strength or stiffness) according to a continuum law. Thus, the dynamics of crack nucleation and growth is not explicitly considered and a mesoscopic description of the failure process is provided. The theoretical premises for the simulation of AE based on elastic damage mechanics were first discussed by Tang *et al.* (1997) and implemented in a finite-element code known as RFPA (Tang 1997). Progressive failure of rock and associated non-linear stress–strain behaviour was captured by an elastic–brittle element constitutive law together with a heterogeneous distribution of the rock parameters. In this context, AE was simulated by a static approach: an acoustic event was associated with each damaged element and the corresponding elastic strain energy dissipation was used as analogous of the released seismic energy. The aforementioned model was used to investigate the evolution of seismic energy release during the failure process of heterogeneous rock specimens in compression (Tang & Kaiser 1998), and to analyse the acoustic activity and the Kaiser effect during a three-point bending test on a concrete beam (Zhu *et al.* 2010). Following similar principles, a number of other models have been introduced. For instance, Fang & Harrison (2002) adopted a local degradation model to analyse the brittle fracture of a rock sample under confined compression and to simulate the associated released energy evolution. Similarly, Feng *et al.* (2006) developed an elastoplastic cellular automata model to simulate the acoustic activity of brittle rock under uniaxial compression. A slightly different approach was developed by Amitrano *et al.* (1999) on the basis of a local scalar damage model with tensorial elastic interaction. In this model, the size of the events was assumed proportional to the total number of elements damaged during a single loading step. The approach was shown to be capable of capturing power-law distributions of damage events in space and size domains, and subsequently adopted to investigate the relationship between seismic *b* value and brittle–ductile transition observed during laboratory tests on granitic rocks (Amitrano 2003). A rheological model accounting for elastic deformation, viscous relaxation

and evolution of damage was introduced by Lyakhovsky *et al.* (1997), which was then used to simulate long histories of crustal deformation and to study the coupled evolution of earthquakes and faults (Lyakhovsky *et al.* 2001).

Particle-based DEM models represent the rock material as an assembly of rigid circular or spherical particles that are bonded together at their contact points. Although a relatively simple set of micromechanical interaction laws is used, these models can reproduce several typical features of the macroscopic rock behaviour including elasticity, fracturing and damage accumulation (Potyondy & Cundall 2004). Crack nucleation is simulated through breaking of internal bonds while fracture propagation is obtained by coalescence of multiple bond breakages. Particle-based DEM models simulate quasi-static deformation by solving the equations of motion. Therefore, elastodynamics effects including stress wave propagation and cracking-induced acoustic emission can be explicitly simulated. Hazzard & Young (2000) developed a technique to dynamically quantify AE in a 2-D bonded-particle model for rocks. Particle kinetic energy upon bond breakage was monitored and used to directly quantify seismic energy radiated from the source. By clustering multiple bond breakages together in space and time, realistic *b* values were obtained for a confined compression test simulation on granite. The aforementioned approach was further improved by introducing moment tensor calculation based on change in contact forces upon particle contact breakage, and was applied to the microseismic simulation of a mine-by experiment in a crystalline rock (Hazzard & Young 2002) and of an excavation-induced fault slip event (Hazzard *et al.* 2002). 3-D simulations of acoustic activity using particle-based DEM were proposed by Hazzard & Young (2004) and Invernizzi *et al.* (2011). While the former represented the direct extension of the 2-D method described earlier, the latter adopted a simplified assumption in evaluating acoustic event size whereby the event magnitude was assumed proportional to the number of broken bonds in a given time interval. Nevertheless, the latter model was able to reproduce the power-law distribution of event size and the decrease of *b* value with increasing applied stress observed during unconfined compression and three-point bending tests on concrete.

A class of methods directly related to the DEM particle models is represented by the lattice (or network) models. Similar to DEM models, continuum constitutive laws are replaced with a mechanical system of springs or beams. However, unlike DEM models, the particle contact pattern is fixed during the simulation and therefore large displacements and deformation cannot be simulated. Heterogeneous material structure is modelled, for instance, by imposing random failure thresholds on the springs or by removing a fraction of the links. Due to their simple description of elasticity and material microstructural disorder, lattice models are only used to provide a mesoscopic description of the general statistics of the fracturing process in brittle and quasi-brittle materials (Alava *et al.* 2006). An example of lattice model based on a scalar damage model was introduced by Zapperi *et al.* (1997). Using the analogy between mechanical fracture and fusion in a resistor network, the model captured amplitudes and intervals between sequential events distributed according to a power law. The amplitude of events was assumed to be equal to the number of links damaged for a given voltage (i.e. stress) increment. Wang *et al.* (2000) developed a static lattice model to study the rock failure and earthquake process. In particular, the effect of crack density, represented by pre-existing broken bonds, on the *b* value was investigated under the assumption of proportionality between event magnitude and potential energy released by a broken bond. Unlike the aforementioned quasi-static approaches, the dynamic model of Minozzi *et al.* (2003) was used to explicitly

analyse the AE waveforms emitted by a propagating crack in a 2-D lattice subjected to antiplanar deformation. The acoustic response was related to the internal damage of the sample, and power-law distributions of acoustic energy were obtained in agreement with experimental observations.

Finally, it is worth mentioning an additional class of models (e.g. Hirose & Achenbach 1991; Lysak 1996; Andreykiv *et al.* 2001; Bizzarri 2011), which focuses on the emission of acoustic waves by solving the elastodynamic problem associated with the initiation and subcritical growth of pre-existing crack-like flaws of idealized shaped (e.g. penny-shaped, disc, ellipse). Based on a continuum fracture mechanics approach, this type of models aims at either quantifying the relationships between crack parameters (e.g. crack area and stress intensity factor) and AE signal (e.g. amplitude and frequency spectrum), or, through the application of self-consistent friction laws, modelling the dynamic rupture of seismogenic faulting processes (e.g. see Bizzarri 2011, for a review).

In the context of the first three classes of methods described earlier, the numerical methodology adopted for this study, namely FEM/DEM, uses continuum mechanics principles and DEM techniques to describe the elastic deformation and the material failure process, respectively. Unlike the majority of the approaches described earlier, the event seismic energy is estimated using a quasi-dynamic technique, which explicitly evaluates the kinetic energy in proximity to spontaneously propagating cracks. Given the mesoscopic representation of the fracturing process by means of cohesive elements, the accurate simulation of dynamic crack propagation and associated phenomena (see Freund 1990) is beyond the scope of this work. Instead, the focus of this paper is on the extraction of quasi-dynamic AE information from a numerical model that aims at capturing the main features of the failure process in brittle rocks (e.g. non-linear stress–strain behaviour, localization of failure).

3 FUNDAMENTAL PRINCIPLES OF FEM/DEM

The combined FEM/DEM is a numerical method pioneered by Munjiza *et al.* (1995) for the dynamic simulation of multiple interacting deformable bodies. The technique combines DEM algorithms that capture the interaction and fracturing of different solids with continuum mechanics principles that describe the elastic deformation of discrete bodies. For this study, a 2-D FEM/DEM code, known as Y-Geo (Mahabadi *et al.* 2012a), was used. This code represents an extension of the original Y2D code of Munjiza (2004) and is undergoing development at the University of Toronto for geomechanical applications. All models illustrated in the following sections were solved under plane stress conditions.

3.1 Governing equations

In FEM/DEM, each solid is discretized as a mesh consisting of nodes and triangular elements. An explicit second-order finite-difference time integration scheme is applied to solve the equations of motion for the discretized system and to update the nodal coordinates at each simulation time step. In general, the governing equations for a FEM/DEM system can be expressed as

$$\mathbf{M\ddot{x}} + \mathbf{C\dot{x}} = \mathbf{R(x)}, \tag{1}$$

where $\mathbf{M}$ and $\mathbf{C}$ are the lumped mass and damping diagonal matrices of the system; $\mathbf{x}$ is the vector of nodal displacements and $\mathbf{R}$

is the nodal force vector which includes the contributions from the external loads, $\mathbf{f}_l$, the interaction forces acting across discrete bodies, $\mathbf{f}_i$, the deformation forces, $\mathbf{f}_e$ and the crack bonding forces, $\mathbf{f}_c$. Numerical damping is introduced in the governing equation to account for energy dissipation due to non-linear material behaviour or to model quasi-static phenomena by dynamic relaxation (Munjiza 2004). The matrix $\mathbf{C}$ is equal to

$$\mathbf{C} = \mu \mathbf{I}, \qquad (2)$$

where μ and $\mathbf{I}$ are the damping coefficient and the identity matrix, respectively.

Interaction forces, $\mathbf{f}_i$, are calculated either between contacting separated bodies or along internal discontinuities (i.e. pre-existing and newly created fractures). In the normal direction, body impenetrability is enforced using a penalty method (Munjiza & Andrews 2000), while in the tangential direction, discontinuity frictional behaviour is simulated by a Coulomb-type friction law (Mahabadi *et al.* 2012a). Deformation forces, $\mathbf{f}_e$, are computed on an element-by-element basis under the assumption of isotropic linear elasticity. Crack bonding forces, $\mathbf{f}_c$, are used to simulate material failure, as further explained in the next section.

3.2 Material failure modelling

The progressive failure of rock material is simulated in FEM/DEM by explicitly modelling crack initiation and propagation according to the principles of non-linear elastic fracture mechanics (Dugdale 1960; Barenblatt 1962). As depicted in Fig. 1, dedicated four-noded cohesive elements simulate the development of the Fracture Process Zone (FPZ), a zone of non-linear material behaviour that

forms ahead of the crack tip due to interlocking and microcracking (Labuz *et al.* 1985). The four-noded cohesive elements (referred hereinafter to as crack elements) are embedded between the edges of 'all' adjacent triangular element pairs from the very beginning of the simulation (i.e. remeshing is not performed as the simulation progresses). Therefore, the potential crack paths do not need to be assumed *a priori* and arbitrary fracture trajectories can be captured within the constraints imposed by the initial mesh topology.

In this study, a modified version of the crack element constitutive response proposed by Munjiza *et al.* (1999) was adopted. The bonding stresses, σ and τ, transferred by the material are decreasing functions of the displacement discontinuity across the crack elements

$$\begin{bmatrix} \sigma \\ \tau \end{bmatrix} = f(D) \cdot \begin{bmatrix} f_t \\ f_s \end{bmatrix}, \qquad (3)$$

where f_t and f_s are the cohesive strengths in tension and shear, respectively, and $f(D)$ is a heuristic scaling function representing an approximation of the experimental cohesive laws proposed by Evans & Marathe (1968).

$$f(D) = \left[1 - \frac{a+b-1}{a+b} \exp\left(D \frac{a+cb}{(a+b)(1-a-b)} \right) \right] \cdot$$
$$\times \left[a(1-D) + b(1-D)^c \right], \qquad (4)$$

where a, b, c are empirical constants equal to 0.63, 1.8 and 6.0, respectively, and D is a damage factor comprised between 0 and 1. As discussed later, the dimensionless damage factor D describes the displacement jump across the cohesive surface. Also, $f(D)$ is such that $f(0) = 1$ (i.e. intact crack element) and $f(1) = 0$ (i.e. broken crack element).
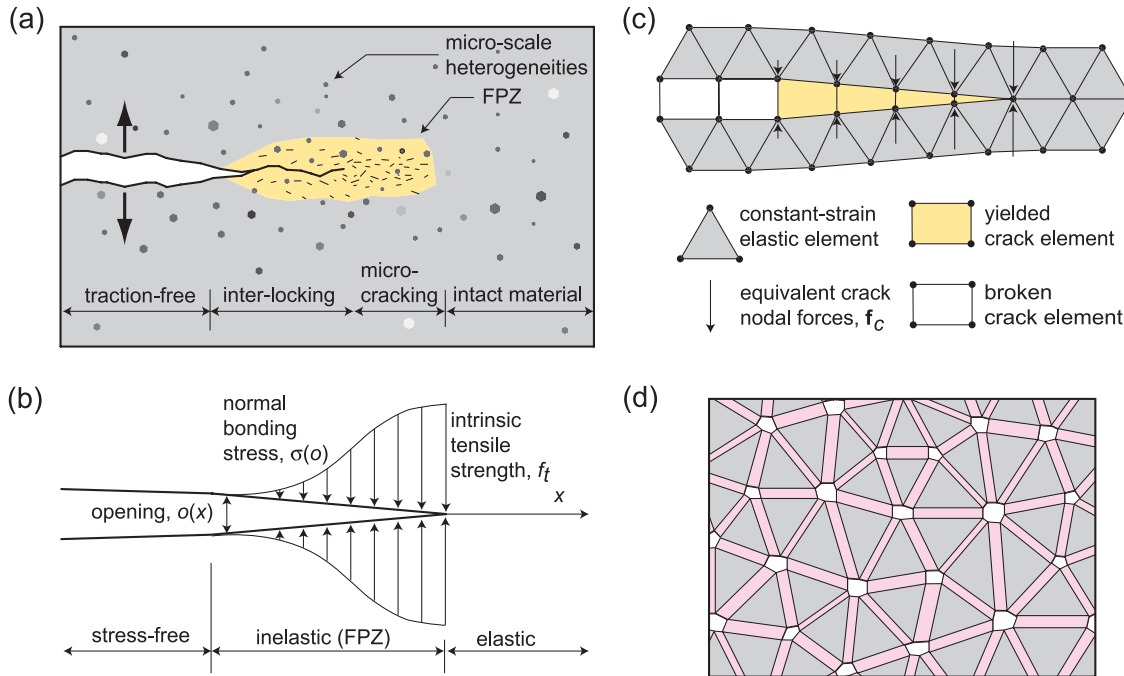
Figure 1. Material failure modelling in FEM/DEM. (a) Conceptual model of a tensile crack in a heterogeneous rock material (modified after Labuz *et al.* 1985). (b) Theoretical FPZ model of Hillerborg *et al.* (1976). (c) FEM/DEM implementation of the FPZ using triangular elastic elements and four-noded crack elements to represent the bulk material and the fracture, respectively. (d) FEM/DEM representation of a fracturable body with continuum triangular elements and embedded crack elements indicated in grey and pink, respectively. Triangular elements are shrunk for illustration purposes. Interpenetration of triangular elements is discouraged by the strong stiffening response of the contact penalty formulation.
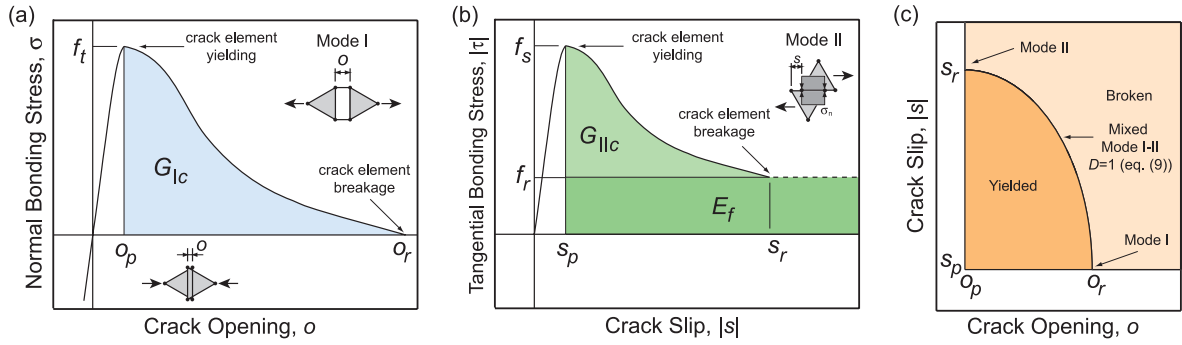
Figure 2. Constitutive behaviour of the crack elements. (a) FPZ model for mode I. (b) Slip-weakening model for mode II. The specific fracture energy values, G_{Ic} and G_{IIc}, correspond to the area under the bonding stress-softening curves. The shape of the curves is based upon experimental complete stress–strain curves obtained for concrete in direct tension (eq. (4), Evans & Marathe 1968; Munjiza *et al.* 1999). Note that the residual shear strength, f_r, is computed according to eq. (7) by the element pair interaction algorithm (Mahabadi *et al.* 2012a) even after the breakage of the embedded crack element (dashed line in b). (c) Graphical representation of the coupling relationship between crack opening, o, and crack slip, s, for mixed-mode fracturing (eq. 9).

Depending on the local stress and deformation field, fractures can nucleate and grow in mode I (i.e. opening mode), mode II (i.e. sliding mode) or in mixed mode I–II. Similar to the cohesive model originally proposed for concrete by Hillerborg *et al.* (1976), a mode I crack initiates when the crack tip opening, o, reaches a critical value, o_p, which is related to the cohesive tensile strength of the rock, f_t (Fig. 2a). As the fracture propagates and the crack tip opening increases, the normal bonding stress, σ, is assumed to decrease until a residual opening value, o_r, is reached and a traction-free surface is created. In this case, the damage factor is therefore defined as

$$D = \frac{o - o_p}{o_r - o_p}. \tag{5}$$

Mode II fracturing is simulated by a slip-weakening model conceptually similar to that of Ida (1972). A tangential bonding stress, τ, exists between the two fracture walls, which is a function of the amount of slip, s, and the normal stress on the fracture, σ_n (Fig. 2b). The critical slip, s_p, corresponds to the cohesive shear strength of the rock, f_s, defined as

$$f_s = c + \sigma_n \cdot \tan\phi_i, \tag{6}$$

where c is the internal cohesion, ϕ_i is the material internal friction angle and σ_n is the normal stress acting across the crack element. Upon undergoing the critical slip, s_p, the tangential bonding stress is gradually reduced to a residual value, f_r, which corresponds to a purely frictional resistance

$$f_r = \sigma_n \cdot \tan\phi_f, \tag{7}$$

where ϕ_f is the fracture friction angle and σ_n is the normal stress acting across the fracture surfaces. The residual shear strength, f_r, is computed according to eq. (7) by the element pair interaction algorithm (Mahabadi *et al.* 2012a) even after the breakage of the embedded crack element. In this case, the damage parameter is therefore defined as

$$D = \frac{s - s_p}{s_r - s_p}. \tag{8}$$

For mixed mode I–II fracturing, the coupling between crack opening and slip is defined by (Fig. 2c)

$$D = \sqrt{\left(\frac{o - o_p}{o_r - o_p}\right)^2 + \left(\frac{s - s_p}{s_r - s_p}\right)^2}. \tag{9}$$

As illustrated in Fig. 1(c), the effect of the crack bonding stress is implemented in FEM/DEM using equivalent crack nodal forces, $\mathbf{f}_c$.

Since the elastic deformation before the onset of fracturing takes place in the bulk material, no deformation should in theory occur in the crack elements before the cohesive strength is exceeded. However, a finite stiffness is required for the crack elements by the time-explicit formulation of FEM/DEM. Such an artificial stiffness is represented by the normal, tangential and fracture penalty values, p_n, p_t and p_f, for compressive, shear and tensile loading conditions, respectively. For practical purposes, the cohesive contribution to the overall model compliance can be largely limited by adopting very high (i.e. dummy) penalty values (Munjiza 2004; Mahabadi 2012).

From an energetic point of view, as there is stress to be overcome in propagating a crack, energy is dissipated during the fracturing process. The material total strain energy release rate, G_c, corresponds to the amount of energy absorbed per unit crack length along the crack edge in displacing a crack from the critical to the residual value. In general, G_c is obtained by integration of the stress-softening curve (represented by eq. (4)) during the debonding process of the crack element and includes the contribution of (i) the surface energy 2γ of the two newly created discontinuity surfaces, (ii) the energy G_d consumed in the damage process around the crack tip and (iii) the frictional fracture energy G_f. G_c is defined in terms of the material properties, G_{Ic} and G_{IIc}, which correspond to the strain energy release rates for modes I and II fracturing, respectively. Therefore, the crack residual displacement values, o_r and s_r, are such that

$$G_{Ic} = \int_{o_p}^{o_r} \sigma(o) \, do, \tag{10}$$

$$G_{IIc} = \int_{s_p}^{s_r} [\tau(s) - f_r] \, ds. \tag{11}$$

Upon breakage of the cohesive surface, the crack element is removed from the simulation and replaced by the interaction forces, $\mathbf{f}_i$, described in the previous section. At this stage, the transition from 'continuum' to 'discontinuum' is complete, finite displacements and rotations of discrete bodies are allowed and new contacts are automatically recognized as the simulation progresses, as typical of the DEM modelling approach (see Cundall & Hart 1992).

4 FEM/DEM SIMULATION OF AE

4.1 Static versus dynamic modelling of crack propagation

During a FEM/DEM simulation, the rock is subjected to certain loading conditions and strain energy is stored due to the elastic

deformation of the triangular elements. Once the intrinsic strength of the material is locally overcome, a new fracture is initiated and the release of stored strain energy begins. As described in Section 3.2, part of this energy is absorbed by the fracturing process itself and its value, G_c, is related to the material input parameters G_{Ic} and G_{IIc}. If the crack surfaces slide against each other in a compressive stress field, part of the released energy is dissipated as frictional work. Frictional stress develops according to eq. (7), while the specific frictional energy dissipated, E_f, depends on the total slip, s

$$E_f = f_r \cdot s. \tag{12}$$

Under static (or quasi-static) conditions, crack extension is therefore governed by

$$G_{stat} = G_c + E_f, \tag{13}$$

where G_{stat} is the static strain energy release rate. As verified in Section 4.3, failure events in FEM/DEM are characterized by an excess of strain energy released with respect to G_c and E_f (i.e. $G > G_c + E_f$), thus the simulated rupture phenomena are often accompanied by the radiation of kinetic energy, E_k, in the form of acoustic emission.

In the framework of continuum fracture mechanics, the mathematical description of the rapid crack propagation process includes the inertial resistance provided by material particles displaced on opposite crack walls (Freund 1990). Under dynamic conditions, the total energy available for work, G_{dyn}, is indeed partitioned into fracture energy, G_c, frictional dissipation, E_f and radiated energy, E_k. That is, an additional kinetic term is added to the energy equation for crack extension as a mean to dissipate the excess energy resulting from the imbalance in the two driving force terms (Kanamori & Brodsky 2004):

$$G_{dyn} = G_{stat} - \frac{1}{2}\frac{\partial E_k}{\partial a}, \tag{14}$$

where a represents the crack area. Then, the crack extension criterion becomes $G_{dyn} = G_c + E_f$ instead of eq. (13). Calculating the radiated energy of a propagating crack is in general a challenging task, which involves computing the displacements as a function of the crack length from the equations of motion for the crack tip in a deformable solid (Lawn 1993). Given the complexities associated with the dynamic stress field and the strain energy flux into the crack tip, simplifying assumptions are generally made. In this context, the rupture speed, V_r, assumes a fundamental importance in determining the ratio of the dynamic to static energy release rate, G_{dyn}/G_{stat}, for a propagating crack. For instance, for a mode I fracture this ratio can be expressed as (Freund 1972)

$$\frac{G_{dyn}}{G_{stat}} = 1 - \frac{V_r}{c_R}, \tag{15}$$

where c_R is the Rayleigh wave speed of the material. Under quasi-static conditions (i.e. $V_r \sim 0$), no energy is radiated and all released strain energy is dissipated in the fracture process zone. Conversely, for rupture speed values approaching c_R, all energy is radiated as seismic energy. Furthermore, the rupture speed, V_r, directly affects the characteristics of the emitted stress wavefield (Section 4.3.7).

The numerical representation of material damage in FEM/DEM is based on a mesoscopic description of the fracturing process using a cohesive crack approach in combination with discrete elements. The elastodynamic problem briefly introduced above is not considered in its entirety and thus the numerical technique does not aim at fully capturing the phenomena occurring during dynamic crack propagation. Nevertheless, quasi-dynamic seismic informa-

tion associated with the brittle failure process can be extracted from a FEM/DEM simulation despite the simplified representation of the fracturing process. The focus of the FEM/DEM technique is on capturing the brittle fracture process, and the validation of the AE modelling methodology relies mainly on the analysis of the emergent AE statistics for a compression test simulation on rock (Section 5).

Two approaches were considered to obtain quantitative information on the acoustic activity of a FEM/DEM simulation. The first approach takes advantage of the discrete representation of the material and of the explicit dynamic solver of the method. This technique, which is described in Section 4.2, is based on the internal monitoring of the node motions during crack propagation. An alternative approach employs the standard seismic source inversion techniques based on traveltimes picked from recordings at selected locations on the edges of the model, as shown in Section 4.3. In general, the latter approach suffers from two major limitations. First, as the simulation progresses, new fractures are generated, more energy is emitted and consequently the level of noise increases. Therefore, to be able to record clearly separated events in time, the model needs to be loaded very slowly resulting in running times that are not acceptable at the moment. Secondly, damage accumulation inside the model results in an extensive loss of continuity which makes waveform analysis impractical after the eventual failure. Nevertheless, if particular fracturing conditions such as those of Section 4.3 are reproduced, the AE information independently obtained by these two methods can be related.

4.2 Internal monitoring of AE sources

The newly developed AE algorithm directly monitors the relative displacement of crack surfaces and records the kinetic energy of nodes in proximity to propagating fractures. As in seismology, for each acoustic event the following parameters can be numerically assessed: (i) source location, (ii) fracture mode, (iii) initiation time and (iv) event seismic energy and magnitude. Note that in the context of this paper the term seismic energy refers to a mesoscopic numerical representation of the actual seismic energy radiated from acoustic events in the fracture process zone.

The breakage of each crack element is assumed to be an acoustic event with location coincident with the centroid of the element itself. The fracture mode is derived from the relative displacement of the fracture edges according to the constitutive behaviour illustrated in Fig. 2. Since crack element failure occurs over a finite time interval, due to its softening behaviour, the assessment of the initiation time is based on the analysis of the kinetic energy of the crack element. It was verified that softening and rupture of a crack element are typically accompanied by the evolution of the kinetic energy of the four crack nodes reported in Fig. 3. The initiation time, T_i, is assumed to be the time at which the kinetic energy of the crack element reaches a maximum.

The associated event seismic energy, E_e, is calculated from the kinetic energy at the initiation time by the following algorithm, similar to the one developed by Hazzard & Young (2000) for a particle-based DEM model:

(1) When the peak strength of a crack element is reached (i.e. the element is yielded), the kinetic energy of the four nodes of the crack element is stored in memory as $E_{k,y}$:

$$E_{k,y} = \sum_{i=1}^{4} m_i v_{i,y}^2, \tag{16}$$
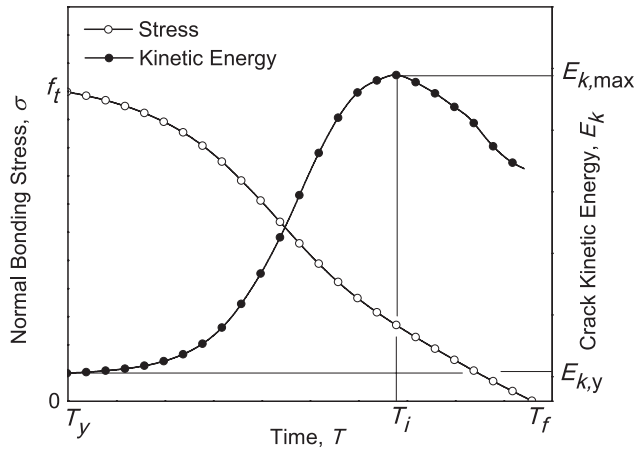
Figure 3. Example of evolution of crack normal bonding stress, σ, and kinetic energy of four crack nodes, E_k, as a function of time, T, for a mode I failing crack element.

where m_i and $v_{i,y}$ are the nodal mass and nodal velocity at the time of yielding $T = T_y$, respectively.

(2) The kinetic energy, $E_k(t)$, of the four nodes is monitored until the crack residual displacement is reached (i.e. the element fails); the change in kinetic energy is calculated at each time step as

$$\Delta E_k(t) = E_k(t) - E_{k,y}. \tag{17}$$

(3) The seismic energy released by each crack breakage is assumed to be equal to the maximum value of ΔE_k attained from the time of yielding, T_y, to the time of failure, T_f, thus corresponding to the initiation time T_i:

$$E_e = \max_{[T_y, T_f]} \Delta E_k(t). \tag{18}$$

(4) Finally, the event magnitude, M_e, can be calculated from the event seismic energy, E_e, using, for instance, the relationship proposed by Gutenberg (1956):

$$M_e = \frac{2}{3} \left(\log E_e - 4.8 \right). \tag{19}$$

It is noteworthy that, at this stage, the technique considers only the seismic energy radiated from the nucleation of new fractures within intact rock material. Thus, the acoustic emissions derived from crack reactivation, such as stress waves generated by slippage along pre-existing discontinuities, are ignored.

4.3 Seismic analysis of AE

The simulation of tensile crack initiation and propagation from a pre-existing flaw was used to investigate the correspondence between the AE information extracted using the technique described in Section 4.2 and that derived from the analysis of recorded synthetic seismograms. The stress concentration induced in a homogeneous medium by the pre-existing crack was exploited to produce strongly localized acoustic events and hence to facilitate the seismic analysis. However, unlike classic fracture mechanics approaches, FEM/DEM does not require in general the presence of crack-like notches or flaws to simulate fracture nucleation and propagation, as illustrated in Section 5.

4.3.1 Model description

The model consisted of a 50 mm × 100 mm homogeneous sample containing a 5-mm long linear flaw inclined at 45° and positioned at the centre of the model (Fig. 4). The sample was discretized by a Delaunay triangulation with an average edge size $h = 0.70$ mm and a total of 21 600 triangular elements.

A constant strain rate was imposed to the model by means of two rigid platens moving in opposite directions at a constant velocity of 0.05 m s^{-1}. This loading rate represented the lowest value that could be used for the given element size while keeping the running time within acceptable limits. A constant integration time step of 5×10^{-9} s was used to solve eq. (1). The material properties reported in Table 1 were assumed for this simulation. The results reported in the following subsections were obtained for a damping coefficient value $\mu = 7.4 \times 10^3$ kg m s^{-1}, which approximates twice the theoretical critical damping, μ_c, assuming that each element of size h (0.70 mm) behaves as a one-degree-of-freedom mass-spring-dashpot system:

$$\mu_c = 2 h \sqrt{\rho E}. \tag{20}$$
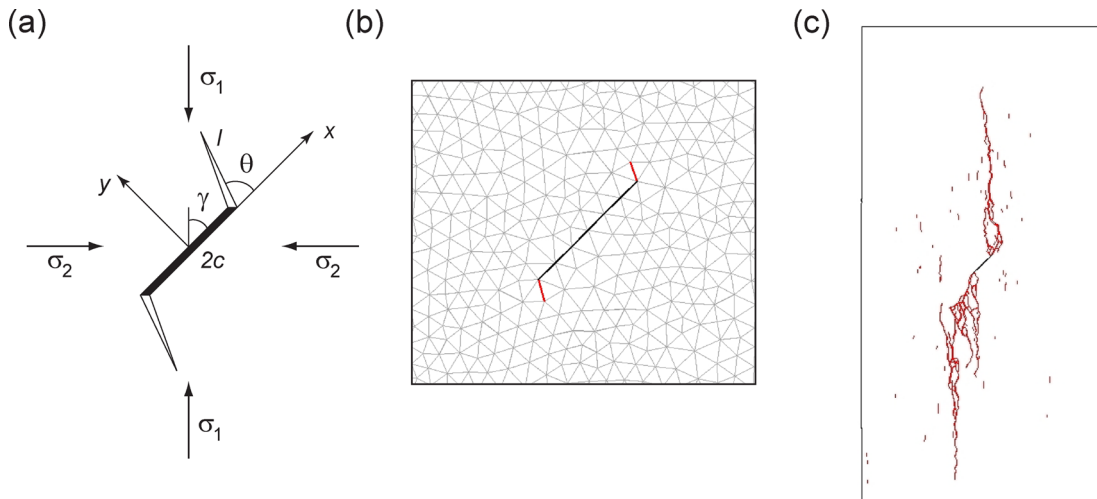
Figure 4. (a) Configuration of a pre-existing straight flaw and tension wing cracks growing in a compressive stress field. (b) Zoomed-in view of the centre of the FEM/DEM model. Top and bottom wing cracks (shown in red), corresponding to acoustic events 1 and 2 (Section 4.3.3), nucleate at $\sigma_{1c} = 7.0$ MPa. (c) FEM/DEM fracture pattern corresponding to the specimen ultimate stress at failure, $\sigma_{1u} = 32$ MPa.

Table 1. Sample properties for the wing crack simulation.

Parameter	Value
Density, ρ (kg m^{-3})	2300
Young's modulus, E (GPa)	3
Poisson's ratio, ν (–)	0.29
Internal friction angle, ϕ_i (°)	35
Internal cohesion, c (MPa)	15
Fracture friction angle, ϕ_f (°)	35
Tensile strength, f_t (MPa)	3
Mode I fracture energy, G_{Ic} (J m^{-2})	2.0
Mode II fracture energy, G_{IIc} (J m^{-2})	10
Damping coefficient, μ (kg m s^{-1})	7.4×10^3
Normal contact penalty, p_n (GPa m)	30
Tangential contact penalty, p_t (GPa m^{-1})	3
Fracture penalty, p_f (GPa)	15
Sample-platen friction coefficient, k (–)	0.1

This value represented an acceptable compromise between noise reduction and AE wave amplitude attenuation, as further discussed in Section 4.3.6.

4.3.2 Analysis of onset of crack growth in the framework of linear elastic fracture mechanics (LEFM)

The nucleation of tension cracks from pre-existing flaws subjected to a compressive stress field and their growth in the direction of maximum compression have been experimentally studied by several authors (e.g. Brace & Bombolakis 1963; Hoek & Bieniawski 1965; Nemat-Nasser & Horii 1982). As discussed by Horii & Nemat-Nasser (1986), this basic micromechanism can be used to explain several features of the failure of brittle rocks, including the transition from axial splitting mode of failure to faulting, if confinement is applied, and the transition from brittle to ductile behaviour, when the confining pressure is suitably large. In the framework of LEFM, this phenomenon is typically analysed with reference to the 2-D configuration illustrated in Fig. 4(a). The model consists of a pre-existing straight crack of length $2c$ immersed in a homogenous, isotropic and linear elastic medium, and subjected to the far-field stresses, σ_1 and σ_2. The flaw is inclined at angle γ to the direction of σ_1 and the extended tension cracks are assumed to be straight lines of length l. A number of approximate, closed-form solutions of this boundary-value problem have been proposed in terms of stress intensity factors, K_I and K_{II}, at the site of wing crack nucleation, and wing crack orientation, θ (see Lehner & Kachanov 1996, for a review). As shown in Fig. 4(b), the FEM/DEM model correctly captures the formation of two tensile fractures nucleating from the flaw tips. These cracks, which are induced by the sliding of the flaw surfaces under unconfined compression ($\sigma_2 = 0$), initiate along two crack elements inclined at angle $\theta = 64°$ to the pre-existing discontinuity. The results of the FEM/DEM simulation were compared to a number of LEFM solutions by computing the applied far-field stress, σ_{1c}, at the onset of wing crack growth with both approaches. In the FEM/DEM simulation, a value of σ_{1c} equal to 7.0 MPa was derived from the nodal reaction forces recorded at the loading platens. This value represented about 21 per cent of the ultimate stress at failure of the specimen, $\sigma_{1u} = 33$ MPa. For the LEFM solutions, σ_{1c} was obtained by imposing the condition

$$K_I(2c, \gamma, \mu, \theta, l, \sigma_1, \sigma_2) = K_{Ic}, \qquad (21)$$

where K_I was calculated for each analytical model using the parameters reported in Table 2 corresponding to the FEM/DEM configura-

Table 2. Parameters used for the wing crack growth analysis using LEFM models.

Parameter	Value
Flaw length, $2c$ (mm)	5
Flaw inclination, γ (°)	45
Flaw friction coefficient, μ (–)	0.7
Wing crack inclination, θ (°)	64
Wing crack length, l (mm)	0.7
Lateral confining pressure, σ_2 (MPa)	0

Table 3. Comparison of compressive stresses at the onset of crack growth, σ_{1c}, obtained using different LEFM models with the FEM/DEM simulation result.

Analysis type	Critical compressive stress, σ_{1c} (MPa)
LEFM model	
Cotterell & Rice (1980)	5.1
Zaitsev (1985)	6.9
Horii & Nemat-Nasser (1986)	14.6
Lehner & Kachanov (1996)	8.5
FEM/DEM simulation	7.0

tion of Fig. 4, and the mode I fracture toughness value, $K_{Ic} = 0.077$ MPa$\sqrt{m}$, was estimated by the following relationship (Irwin 1957):

$$G_{Ic} = \frac{K_{Ic}^2}{E}, \qquad (22)$$

where E and G_{Ic} are the Young's modulus and mode I fracture energy release rate, respectively (Table 1). The comparison of σ_{1c} values reported in Table 3 indicate that the FEM/DEM result falls within the range predicted by the different LEFM models. Discrepancies between solutions are due to varying modelling assumptions within the LEFM models (Lehner & Kachanov 1996) and between the LEFM and FEM/DEM approaches. In particular, the LEFM theory is underpinned by the lack of a plastic zone at the tip of a crack which implies a fully elastic behaviour with stress singularities. Conversely, in FEM/DEM, an FPZ develops ahead of the crack tip once the cohesive strength is reached (Section 3.2). Also, the angle of crack propagation in the FEM/DEM cohesive fracture model is constrained along the edges of triangular elements and the details of the crack tip stress and strain fields are not resolved by the relatively coarse numerical discretization with constant-strain elastic elements (Fig. 4b).

As the simulation progresses, the two fractures tend to align themselves in the direction parallel to the maximum principal stress. The eventual failure of the sample involves the development of secondary shear fractures and macroscopic axial splitting (Fig. 4c).

4.3.3 Simulated AE

The above described wing cracking process was accompanied by the radiation of kinetic energy from the two tensile fractures, as preliminarily indicated by the simulated evolution of particle velocity field in the sample (Fig. 5). Hence, the synthetic acoustic activity was simultaneously monitored using the technique illustrated in Section 4.2 and two sets of receivers positioned on the left and right side of the sample (Fig. 6a). Particle velocities were recorded at these receivers to mimic the effect of piezoelectric transducers used in actual AE experiments.
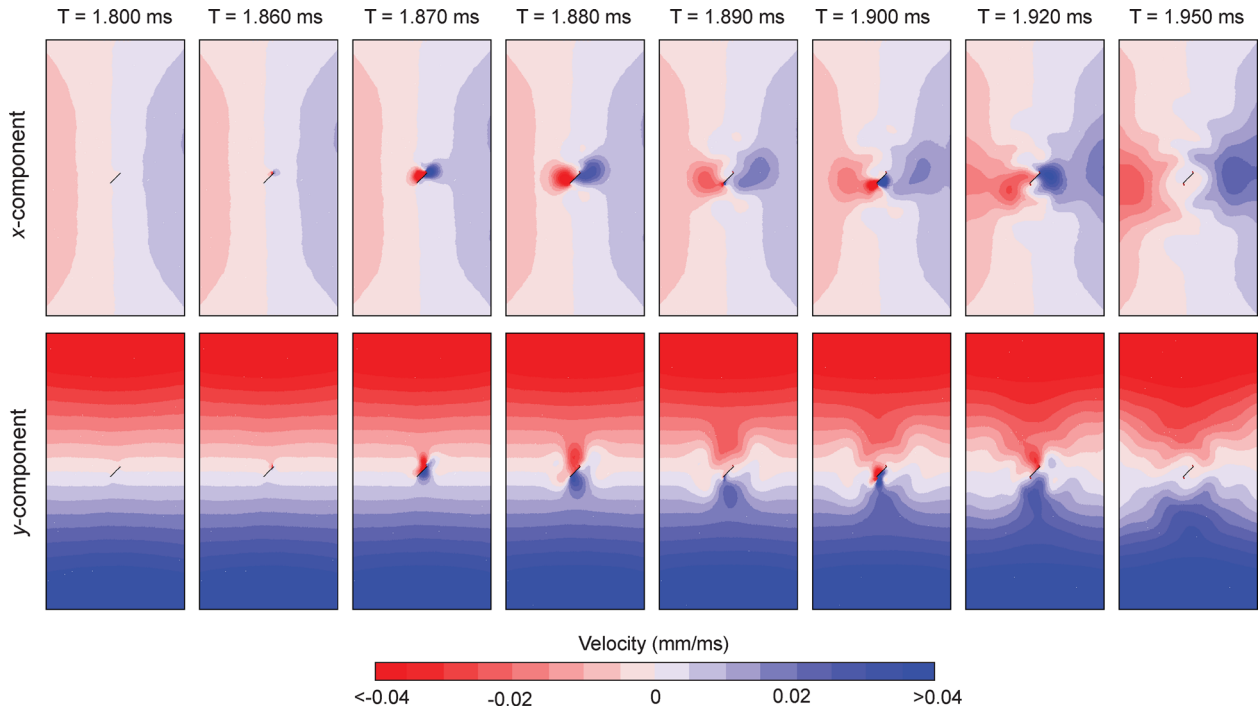
Figure 5. Contour plot of *x*- and *y*-components of particle velocity in the sample for $T = [1.800, 1.950]$ ms of the wing crack propagation simulation. Background velocity field prior to fracturing ($T = 1.800$ ms) is induced by the loading platens moving in opposite direction with a constant vertical velocity of $0.05 \, \text{m s}^{-1}$. The lateral expansion of the sample is due to the Poisson's effect. Note also the constraint placed on the lateral deformation at the top and bottom sample boundaries by the frictional resistance of the platen-sample interface. Two fracture-induced energy releases occur at $T = [1.860, 1.870]$ and $T = [1.890, 1.900]$ ms. These events are associated with two new fractures nucleating from the top and bottom tip of the pre-existing crack and correspond to events 1 and 2 of Fig. 6(b), respectively.
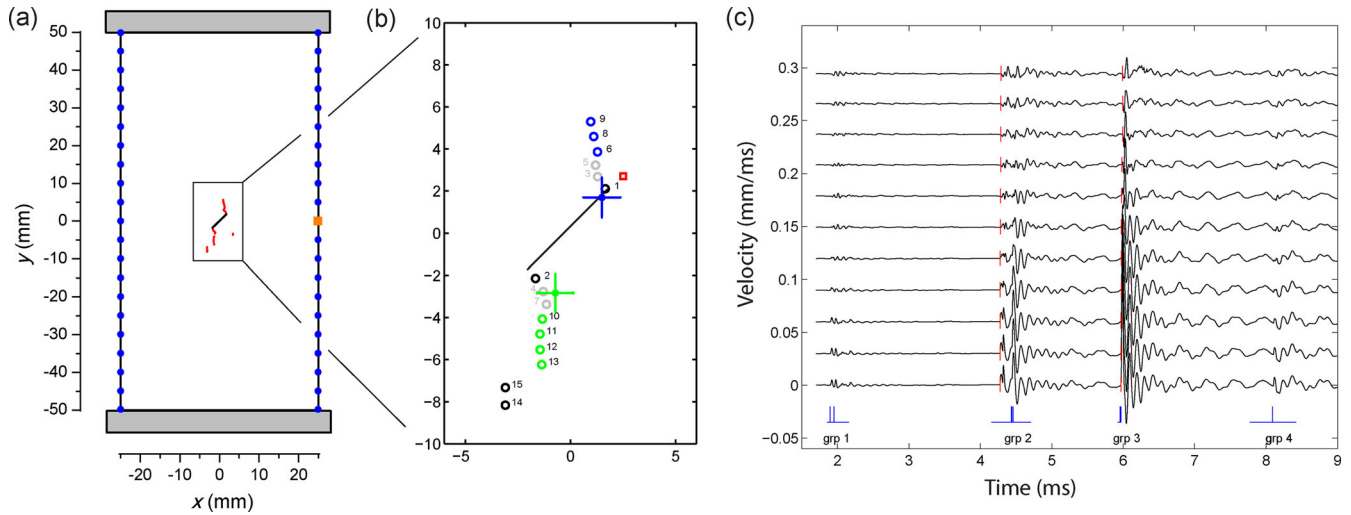
Figure 6. (a) Model and receiver geometry for the wing crack propagation simulation together with simulated fracture (i.e. source) pattern. The broken crack elements (shown in red) cluster in two macroscopic fractures originating from the tips of the diagonal flaw. Two sets of receivers placed on the left- and right-side edges are indicated by blue dots. The location of the receiver [25, 0.0] mm discussed in Sections 4.3.5 and 4.3.6 is indicated by an orange square. (b) A zoomed-in view of the centre of the sample showing the associated acoustic events in circles; minor events with $E_e \leq 1$ nJ are denoted by grey circles and major events are in black (for groups 1, 4), blue (for group 2) and green (for group 3) circles. Inverted event locations based on manual traveltime picks for groups 2 and 3 and their associated error bars are indicated by blue and green crosses. Note the proximity between the FEM/DEM major event locations and inverted locations. The virtual receiver at [2.5, 2.7] mm discussed in Section 4.3.6 is indicated by a red square. (c) *x*-Component record section of velocity seismograms between 2 and 9 ms for the top half of the receivers on the right edge. Seismograms have been shifted along *y*-axis to allow proper display. Time ranges for the four event groups recorded by the FEM/DEM modelling (listed in Table 4) are identified below the recorded section with peak times of individual events indicated by vertical lines. The manually picked first arrivals for groups 2 and 3 are indicated by red vertical lines. All seismograms are of the same scale and the maximum amplitude of the bottom velocity seismogram between 4 and 5 ms is $0.04 \, \text{m s}^{-1}$.

Table 4. Event groups for the analysis of the record section for the wing crack simulation. Major events are identified as events with significant internally recorded energy (i.e. $E_e > 1$ nJ), while rest of the events within the defined time ranges are listed under minor events.

Group number	Time range (ms)	Major events	Minor events
1	[1.8, 2.02]	events 1, 2	
2	[4.1, 5.0]	events 6, 8, 9	events 3, 5
3	[5.8, 6.7]	events 10, 11, 12, 13	events 4, 7
4	[7.7, 8.5]	events 14, 15	

4.3.4 Traveltime inversions of acoustic emission

The main arrivals of various AE events cluster in time, as highlighted by the *x*-component record section (Fig. 6c) for the top half of receivers at the right-side edge (Fig. 6a). In particular, four distinct event groups may be identified from the record section before the catastrophic failure of the sample at $T = 9$ ms, corresponding to a sharp increase of fracture nucleation within the model (Fig. 4c). Based on the internally recorded energy by FEM/DEM, each group consists of major (i.e. $E_e > 1$ nJ) and minor (i.e. $E_e \leq 1$ nJ) events as listed in Table 4. Since events within each group may arrive close in time (Fig. 6c), a distinction of individual events can be difficult.

On the other hand, Fourier analysis of the record section showed dominant frequencies of 8–10 kHz (also see more discussions in Sections 4.3.6 and 4.3.7). With a V_p value of 1300 m s^{-1} (calculated from the elastic properties of Table 1), the dominant wavelengths of seismic waves at the receivers were 130–165 mm, far exceeding the dimensions of the sample. Therefore, mapping fracturing details based on backprojection or adjoint-type of source imaging techniques (e.g. Ishii *et al.* 2005; Hjörleifsdóttir 2007) was precluded, as their imaging resolution is generally similar to the dominant wavelength of seismic waves. Seismic event relocation had to rely mainly on the picking of phase onset corresponding to first arrivals of events. However, the close temporal proximity of events within each group and the long-period nature of the recordings limited the picking exclusively to first arrivals for each event group, and in turn provided hints to the location and origin time of only the first event of significant energy in each group.

First arrival times for event groups 2 and 3 were hand-picked, as shown by the red vertical lines in Fig. 6(c). The error bar assigned to the arrival times at each receiver was estimated from the difference between the *x*- and *y*-component time picks with a minimum of 0.001 ms for group 2 and 0.002 ms for group 3 (Fig. 7). A higher minimum error bar was necessary for group 3 due to the preceding ringings from the coda waves of group 2. Larger error bars are generally observed for stations that are further away from the wing crack as the diminishing amplitudes of the first arrivals reduce the accuracy of the phase onset picking (Figs 6c and 7).

With first arrival times picked for 42 receivers on the left and right edges, both event origin times and locations were inverted based on a homogeneous and isotropic background model with a *P*-wave velocity of 1300 m s^{-1}. Arrival data were weighted by the associated error bars, and errors on inverted origin times and locations were computed based on data variance estimation from the goodness of fit. The inverted event origin time (circles in Fig. 8) falls between the yielding time T_y and peak time T_i of the first major event in each group reported by FEM/DEM modelling. The inverted locations with their associated error bars (crosses in Fig. 6b) clearly overlap with the earlier minor events within each group (i.e. events 3 and 4 in groups 2 and 3, respectively), and are only slightly off from the locations of the first major events (i.e. events 6 and 10 in groups 2 and 3, respectively). Given the systematic errors associated

with the assumption of homogeneous isotropic background model and the uncertainties in the phase-picking itself, error bars of the inverted locations may be underestimated. Overall, the seismically inverted event origin times and locations seem to coincide with the first major event (or earlier minor events) in each event group, thus validating the recordings of acoustic emission.

4.3.5 Energy scaling

It will also be interesting to estimate the radiated seismic energy of AE events based on recorded velocity seismograms at receivers, and compare it to the seismic energy E_e computed from eq. (18) based on the source kinetic energy (see Section 4.2). An event that is of larger magnitude and records higher kinetic energy in general also releases more radiated seismic energy. However, again owing to the large damping value and long-period nature of the arrivals on model edges, it is difficult to estimate the absolute radiated seismic energy, and only relative scaling of seismic energy among different events can be compared in the attempt to validate the FEM/DEM calculations.

On the other hand, due to the spatial and temporal proximity of events in an event group (see Table 4), only the total or average seismic energy for an event group can be examined. The instantaneous seismic energy density at a receiver x_r as a function of time is given by

$$E_{is}(x_r, t) \sim \rho[V_x^2(x_r, t) + V_y^2(x_r, t)], \tag{23}$$

where V_x and V_y are the *x*- and *y*-component velocity series recorded at x_r, and ρ is the density of the sample reported in Table 1. A qualitative scaling relation is visible between the instantaneous seismic energy density, $E_{is}(t)$, for the middle receiver on the right-side edge (orange square in Fig. 6a), and the total seismic energy (i.e. sum of E_e for all events within the group) reported by FEM/DEM (Fig. 9a). A less crude estimate of radiated seismic energy density requires temporal averaging and spatial integration of the instantaneous energy density for all receivers by

$$E_s \sim \frac{\rho}{2\pi T_g} \int_t \sum_r \left[V_x^2(x_r, t) + V_y^2(x_r, t) \right] \Delta\theta_r \, dt. \tag{24}$$

The time integration is done over a length of T_g covering the few oscillations after first arrivals, and $\Delta\theta_r$ is the azimuthal angle spanned by neighbouring receivers. As we only seek relative comparisons of radiated energy among different event groups, common factors such as attenuation and geometric spreading are ignored. A linear scaling is observed between the total seismic energy estimated for each event group using eqs (24) and (18) (Fig. 9b), thus helping validate the calculation of the event seismic energy based on the source kinetic energy monitoring performed in the FEM/DEM modelling.

4.3.6 Effect of numerical damping

A uniform viscoelastic damping was applied to all triangular elements of the model to dissipate the transient oscillations induced by the moving loading platens and the actual AE sources that would have otherwise been trapped indefinitely within the modelling domain. This numerical damping, together with the geometric spreading effect, reduces the amplitudes of arrivals as seismic waves travel further from the source region, as indicated for instance by the decrease of first arrival amplitudes for receivers towards the top of the right edge for both event groups 2 and 3 (Fig. 6c).
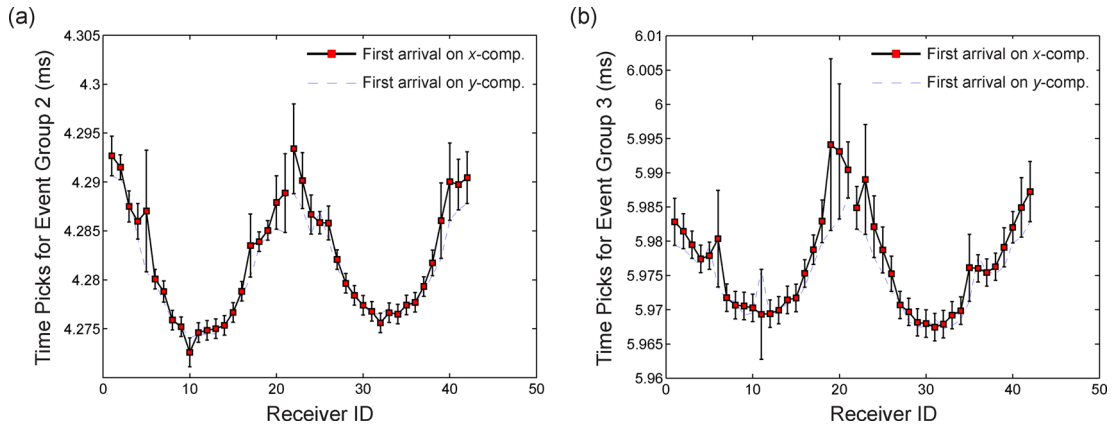
Figure 7. First arrival picks of *x*- (black) and *y*-components (blue) for (a) event group 2 and (b) event group 3 for receivers at the left (receiver ID 22–42) and right (receiver ID 1–21) edges of the model domain. Error bars are given by the discrepancy of *x*- and *y*-component picks with a minimum of 0.001 and 0.002 ms for event group 2 (graph a) and group 3 (graph b), respectively.
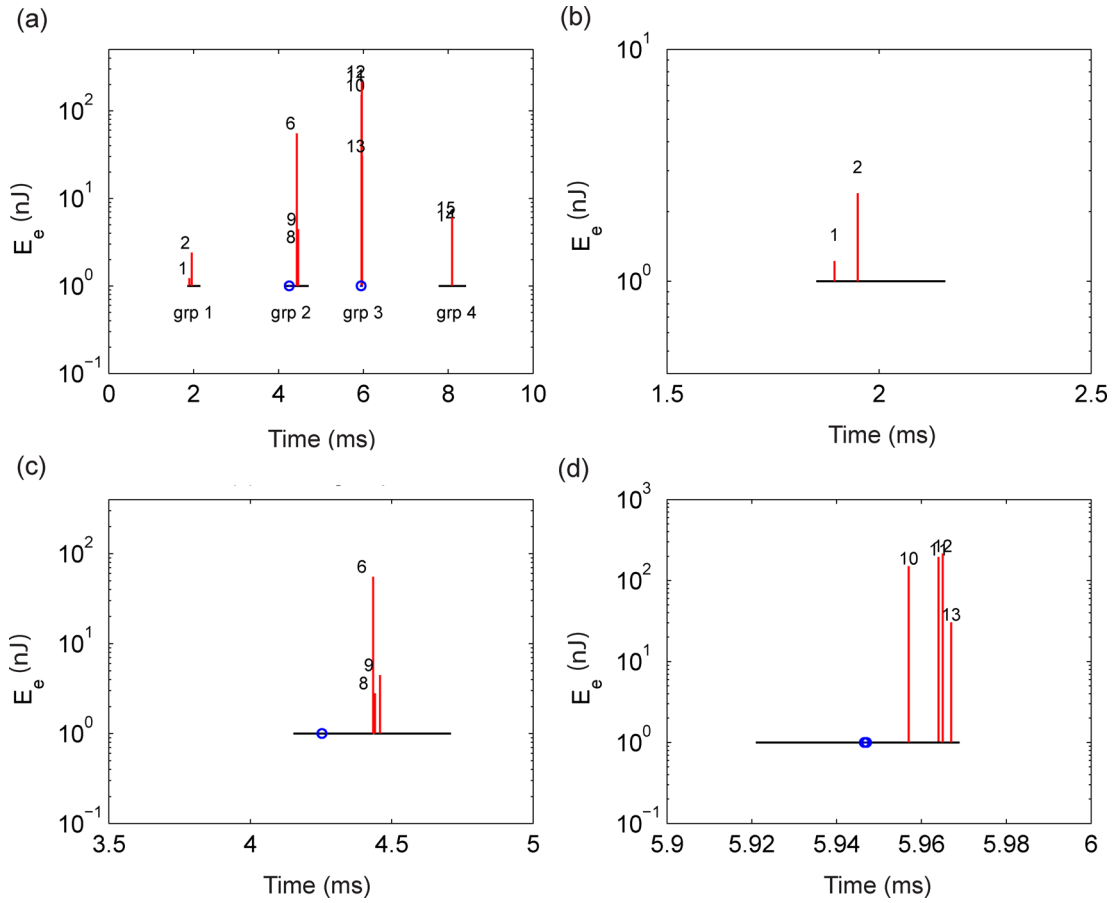

Figure 8. (a) Temporal distribution of AE events reported by FEM/DEM modelling and divided into four event groups. The origin times for event groups 2 and 3 are inverted, each given by two circles indicating the error bar associated with the estimate. However, time errors are generally very small, and the two circles practically overlap. The time extent $[T_y, T_f]$ of major events are indicated by horizontal lines with internally recorded seismic energy, E_e (eq. 18), plotted as vertical lines at their peak times, T_i. (b)–(d) Close-up views of (a) for event groups 1, 2 and 3.

Higher damping values result in more reduction of AE amplitude and attenuation of high-frequency content, as highlighted by the *x*-component particle velocities during events 1 and 2 (Fig. 10a) and by the corresponding amplitude spectra (Fig. 10b), respectively. For comparison, the recordings of a receiver (black line in Fig. 10a) close to the AE source of event 1 ([2.5, 2.7] mm) are less affected by the selection of damping value and geometrical spreading, and

hence more accurately represent the source time functions of individual events in the fracture process. Its spectrum indicates that the dominant frequencies of the source processes are about 10–20 kHz and not much energy is present above 60 kHz (black line in Fig. 10b).

The critical damping value as expressed by eq. (20) is based on the assumption that each triangular element behaves as a
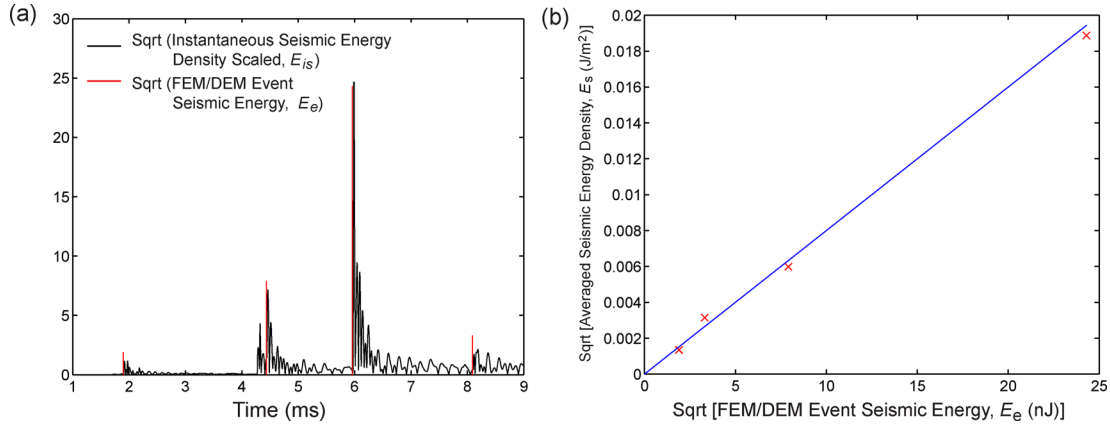
Figure 9. (a) A qualitative linear scaling relation between instantaneous seismic energy density, E_{is}, estimated for the centre receiver on the right side of the sample (i.e. orange square in Fig. 6a) and the total seismic energy, E_e, calculated by internal kinetic energy monitoring, for all four event groups (see Table 4). The total seismic energy values are plotted at the peak times of each event group. Squares of energy values are taken to better present four event groups on the same graph. (b) Linear scaling relation between the squares of seismic energy, E_s, estimated from receiver recordings and seismic energy, E_e, calculated by internal kinetic energy monitoring, shown by the red symbols $\times$ for four event groups and a best fitting line.
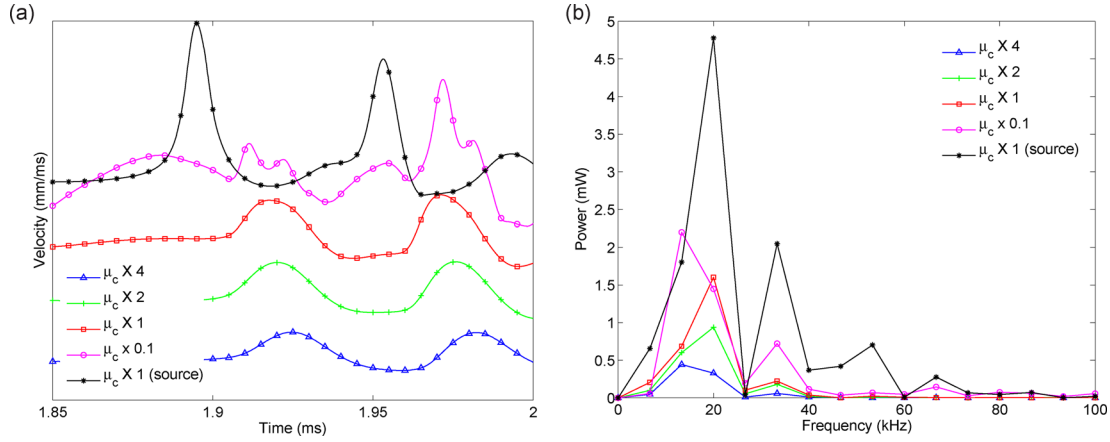
Figure 10. (a) Velocity seismograms recorded for a receiver on the middle of the right edge [0, 25] mm (i.e. orange square in Fig. 6a) at $4\times, 2\times, 1\times, 0.1\times$ the critical damping value ($\mu_c = 3.7 \times 10^3$ kg m s^{-1}) used in FEM/DEM modelling for events 1 and 2. Velocity seismogram of a receiver located at [2.5, 2.7] mm close to the sources of event 1 (i.e. red square in Fig. 6b) for a simulation with critical damping value is also shown. All seismograms are of the same scale and the maximum amplitude of the bottom velocity seismogram is 0.01 m s^{-1}. Symbols are plotted every 1000 data points only. Note the noise in the signal induced by the loading platens for $\mu = 0.1 \times \mu_c$. (b) Amplitude spectra of velocity seismograms in (a).

mass-spring-dashpot system (see Section 4.3.1). Therefore, theoretically, for waves excited at the sources, damping is most significant at frequencies

$$f \gtrsim \frac{E}{2\pi \mu_c}. \tag{25}$$

It then follows that for a simulation with parameter values listed in Table 1 and twice the critical damping μ_c, AE events will mostly generate oscillations below 60 kHz (Fig. 10b). Even at this frequency limit, it is still difficult to image individual events based on backprojection or adjoint techniques, as locating individual events accurately at submillimetre scale would require frequency content above $\sim$1.3 MHz. On the other hand, a further reduction in applied damping will result in unwanted persistent oscillations induced by the moving platens and will therefore hamper the seismic analysis.

Finally, although damping affected the recorded waveforms, it was verified that, under the given loading rate, the failure load of the sample was relatively insensitive to this parameter. In other words, breakages of crack elements triggered by acoustic energy (i.e. dynamically) can be neglected.

4.3.7 Rupture speed and AE frequency content

A qualitative explanation of the aforementioned low-frequency content of the AE source processes may be provided by considering the propagation speed, V_r, of the simulated fractures. For example, events 6, 8 and 9 (i.e. group 2) can be interpreted as a single crack of length $l = 3 \times h = 2.1$ mm. By approximating the duration of crack propagation as $T_{f,9} - T_{y,6} = 0.55$ ms, a rupture speed of about 4 m s^{-1} is estimated. A similar analysis for the other sequences of events reveals rupture speed values comprised between 2.5 and 55 m s^{-1}. The low values of rupture speed in the FEM/DEM simulation (i.e. $V_r \sim (0.004 - 0.1)c_R$) imply that most of the released energy is dissipated in the process zone as fracture energy (eqs 14 and 15) and that high frequencies are not generated at the source (Fig. 10b) as a result of low accelerations of relative displacements along crack elements.

This quasi-dynamic behaviour is a direct consequence of the mechanical assumptions inherent in the cohesive crack approach (Section 3.2). More specifically, the bonding stress-softening relationships depicted in Fig. 2 lump into a discrete line the effect of inelastic mechanisms, including acoustic events, that, in reality,

characterize a finite volume of material ahead of the crack tip (i.e. the FPZ, Fig. 1a). As a consequence, the simulated AE signals are directly influenced by this mesoscopic representation of the process zone, for which the advancement rate is relatively slow. Conversely, acoustic signals measured in the laboratory are due to the multitude of dynamic microfailures within the FPZ itself. As experimentally shown by Zietlow & Labuz (1998), these events may be related to the presence of microscale inhomogeneities in the material such as mineral grains and pre-existing defects or voids. Owing to the truly dynamic nature of these microcrack propagation phenomena and their submillimetre size, much higher frequencies (e.g. 100 kHz–2 MHz, Lockner 1993) are typically measured in the laboratory.

5 NUMERICAL EXAMPLE: AE OF A GRANITE SAMPLE UNDER UNCONFINED COMPRESSION

A model of uniaxial compression test was adopted to investigate the acoustic activity associated with the failure process of a heterogeneous crystalline rock, namely Stanstead Granite, and to provide further validation of the FEM/DEM-AE modelling technique.

The mechanical properties of the FEM/DEM model were first calibrated to reproduce the macroscopic stress–strain response observed during standard laboratory tests. The acoustic activity associated with fracturing was then analysed with particular emphasis on (i) the relation between AE and sample stress–strain response, (ii) the frequency–magnitude statistics and (iii) the spatial clustering of AE sources. Since experimental measurements of AE were not available, the results reported in the following are discussed with reference to the typical behaviour reported in the literature for granitic rocks.

5.1 Model description

The modelled rock sample cross-section consisted of a 54 mm × 108 mm rectangle, meshed with a uniform, unstructured grid having 0.8 mm average element size and totalling approximately 16 000 tri-

angles. Uniaxial loading conditions were obtained by means of two rigid platens moving in opposite directions with a constant velocity equal to 0.125 m s^{-1}, which corresponds to a strain rate of 2.3 s^{-1}. Although in actual experiments the sample is loaded at a significantly slower rate, a preliminary analysis revealed that the possible error in the simulated peak strength due to the different loading rate was bound to 0.5 per cent (Mahabadi 2012). That is, the simulated strengths approached constant values for loading rates smaller than approximately 0.125 m s^{-1}, which thus defined the upper boundary of quasi-static loading conditions of the simulation. Conversely, hardening effects were captured for higher strain rate values (i.e. dynamic range). More details on the FEM/DEM simulation of strain rate effects under true dynamic conditions can be found in Mahabadi *et al.* (2010a). Equations of motion for the discretized system were integrated with a time step of 5×10^{-6} ms; this value was the largest time step size that ensured numerical stability for the explicit time integration scheme of the code. The FEM/DEM Graphical User Interface Y-GUI (Mahabadi *et al.* 2010b) was used to assign boundary conditions and material properties to the model.

The heterogeneous spatial distribution of mineral phases was stochastically generated based on a discrete Poisson distribution of the rock mineral composition with 71 per cent feldspar, 21 per cent quartz and 8 per cent biotite (Fig. 12a). Material properties adopted for each mineral are summarized in Table 5. To simulate the presence of defects within the rock microstructure, the mode I fracture energy values, G_{Ic}, for the interfaces between biotite and feldspar, biotite and quartz and quartz and feldspar were reduced to 0.05, 0.05 and 0.6 J m^{-2}, respectively. Note that an equivalent homogeneous distribution of material properties would have resulted in the inability of reproducing any localized crack element failure (i.e. acoustic event) before the macroscopic rupture of the sample. As typical of the DEM modelling methodology, following an iterative calibration procedure, friction, cohesion and tensile strength of the rock mineral interfaces were varied until the emergent Uniaxial Compressive Strength (UCS) of the model closely matched the value obtained from laboratory testing. Normal contact penalty, tangential contact penalty and fracture penalty values were assumed equal to 10×, 1× and 5× the Young's modulus value, respectively (Mahabadi 2012).

Table 5. Mineral properties of the Stanstead Granite sample for the uniaxial compression test simulation.

Property	Feldspar	Quartz	Biotite
Volume fraction (per cent)	71 per cent[a]	21 per cent[a]	8 per cent[a]
Density, ρ (kg m^{-3})	2600[b]	2600[b]	2800[b]
Young's modulus, E (GPa)	56.4[c]	83.1[c]	17.2[c]
Poisson's ratio, ν (–)	0.32[b]	0.07[b]	0.36[b]
Internal friction angle, ϕ_i (°)	51.8[d]	51.8[d]	51.8[d]
Internal cohesion, c (MPa)	24.2[d]	24.2[d]	24.2[d]
Tensile strength, f_t (MPa)	5.5[e]	11.4[e]	4.2[e]
Mode I fracture energy, G_{Ic} (J m^{-2})	310[f]	907[f]	599[f]
Mode II fracture energy, G_{IIc} (J m^{-2})	620[g]	1814[g]	1198[g]
Platen-mineral friction coefficient, k (–)	0.1[h]	0.1[h]	0.1[h]

[a]From thin section and μCT analysis (Mahabadi 2012).

[b]From Mavko *et al.* (2009).

[c]Measured by microindentation testing (Mahabadi 2012; Mahabadi *et al.* 2012b).

[d]Average (bulk) rock value from uniaxial and biaxial compression testing (Mahabadi 2012).

[e]Estimated by scaling the bulk tensile strength of the rock using the fracture toughness values: $f_{t,min} = f_{t,rock} \cdot K_{Ic,min}/K_{Ic,rock}$.

[f]Estimated from values of mode I fracture toughness, K_{Ic}, measured by microindentation testing (Mahabadi 2012) ($G_{Ic} = K_{Ic}^2/E$).

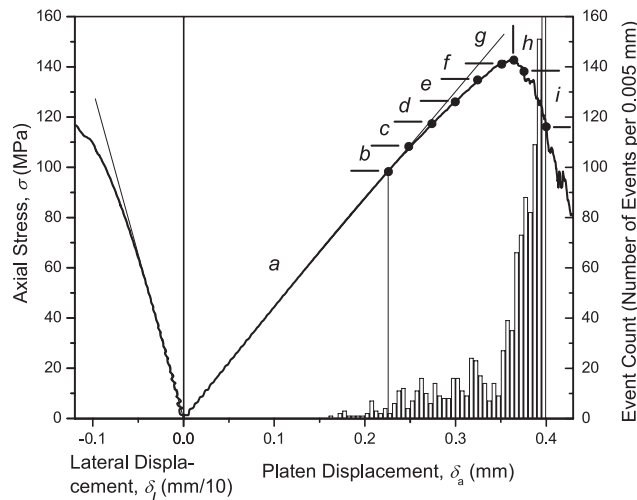[g]Assumed equal to $2 \times G_{Ic}$.

[h]Assumed equal to 0.1.

A critical viscous damping was applied to the model. Further details on the model calibration procedure and experimental results can be found in Mahabadi (2012).

Since the quality of AE seismograms was heavily influenced by the high loading rate and the relatively diffuse damage pattern, temporally separated events could not be recorded, and thus a seismic analysis, as explained earlier in Section 4.3, was not realized. Therefore, AE analysis had to rely only on the internal monitoring of AE sources (Section 4.2).

5.2 Stress–strain behaviour and acoustic activity

Emergent UCS value, Young's modulus and Poisson's ratio of the sample are equal to 142.9 MPa, 49.7 GPa and 0.25, respectively. These values are in good agreement with the respective experimental values of 147.3 MPa, 52.5 GPa and 0.23, used as calibration targets. The onset of AE coincides with the initiation of non-linearity in the lateral strain curve while, in the axial direction, the response of the model is linear until a displacement of about 0.250 mm is reached (stages *b* and *c*, Fig. 11). With increasing applied strain, more crack elements start to break, more damage is accumulated and acoustic energy emitted, resulting in the load-displacement curve beginning to deviate from linearity. Further increase of displacement leads to an increase in the acoustic event count (stages *c* to *f*). Cracking in the pre-peak non-linear stage is diffuse over the sample surface and dominated by extensional failure type (Figs 12b–f). Furthermore, the friction at the interface between rock sample and platens effectively constrains the lateral deformation of the rock sample and, therefore, fracturing tends to be inhibited in the lower and upper part of the sample. Analysis of failure type distribution in stages *a* to *e* (Fig. 13) indicates that the microfracturing process within the crystalline structure of the numerical sample correlates exclusively with the breakage of weaker interfaces at the biotite–feldspar and biotite–quartz contacts.

As the sample approaches its peak strength, a sensible increase in the acoustic event count is recorded (stage *g*) (Fig. 12 e). In this stage, 10 and 1 per cent of the events occur at the stronger quartz–feldspar interfaces and within the feldspar, respectively. Finally, the post-peak behaviour is characterized by a sharp increase in the AE count (stages *h* and *i*), which leads to the sudden loss of sample strength that is typical of brittle failure in rocks. The corresponding fracture pattern (Fig. 12 f) is characterized by the coalescence of vertically aligned cracks into a macroscopic throughgoing fracture plane that extends from the bottom right corner to the top of the sample and by boundary-parallel extensional fractures in the sample left side. A sensible increase of quartz–feldspar intergranular (35 per cent on average) and intragranular (8 per cent on average) failures were recorded in stages *h* and *i*. Beyond $\delta_a = 0.4$ mm, no meaningful AE information could be extracted from the model. Due to the lack of lateral confinement and the rock brittle behaviour, the recorded AE is heavily influenced by the kinetic energy associated with the sample fragmentation (e.g. high-speed lateral ejection of detached rock spalls). This kinetic energy is clearly non-representative of the actual acoustic activity.

5.3 Frequency–magnitude distribution of AE

The AE amplitude distribution during fracturing experiments has been shown to obey the Gutenberg–Richter relationship (Richter 1958) observed for crustal earthquakes (Mogi 1962; Scholz 1968a). Based on this relationship, the distribution of AE size can be expressed by a power law:
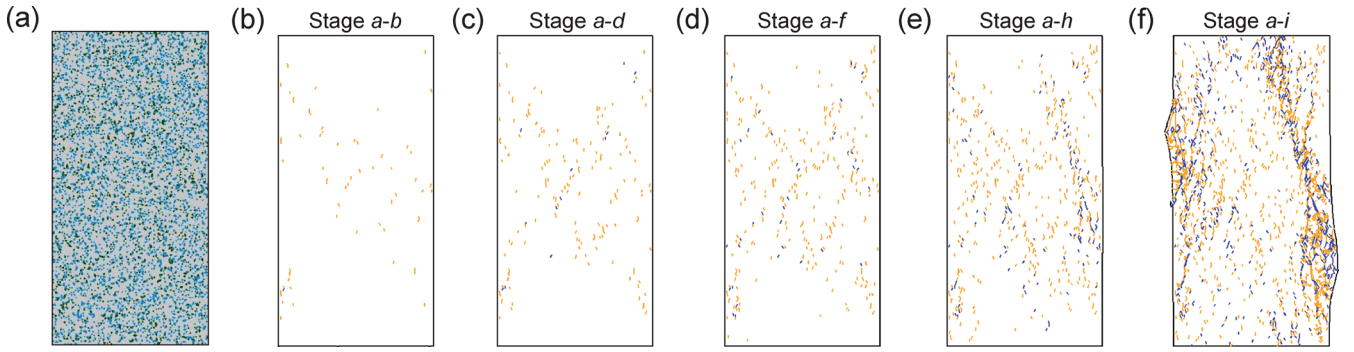
$$N(> A) = a A^{-b}, \tag{26}$$

where A is the maximum amplitude of AE, N is the number of events with amplitude greater than A and a and b are constants. In logarithmic coordinates, this relationship becomes linear.

$$\log N(> M) = a - bM, \tag{27}$$

where $M = \log A$ is the AE magnitude and the exponent b represents the scaling of AE magnitude distribution. The evolution of b value has been studied to diagnose the fracture development stage during laboratory testing of rock samples (e.g. Lockner *et al.* 1991) and in non-destructive testing of structures (e.g. Carpinteri & Bocca 1991). In earthquake seismology, the b value analysis has been used as an earthquake forecasting tool (e.g. Mogi 1967). In this study, the evolution of b value during the UCS test simulation was analysed with reference to the nine axial consecutive displacement windows (stages *a* to *i*) shown in Fig. 11. Event magnitudes were calculated from the kinetic energy of the AE sources using eqs (18) and (19). Since in actual AE monitoring the size of AE recorded is limited by the resolution, synthetic AE events with magnitude smaller than -9.0 were excluded from the calculation.

The frequency–magnitude distributions (Fig. 14) show a good linear behaviour from stages *a* to *f*, corresponding to the linear and non-linear pre-peak portions of the stress-displacement curve. In the peak and post-peak intervals (stages *g* to *i*), a marked increase in the mean event magnitude and number of events is accompanied by a loss of linearity in the distributions, which tend to exhibit a large magnitude cut-off indicative of the presence of a finite-size effect. In other words, when the applied stress, σ, is <97 per cent of the failure stress (up to stage *g*), the AE population is relatively small and the distribution is fully linear over the entire range of magnitude. For higher applied stresses and in the post-peak region, a polynomial fit would provide a better correlation between event

Figure 11. Axial stress, σ, versus platen displacement, δ_a, and lateral displacement, δ_l, for the UCS test simulation, also showing counts of acoustic events as columns. Letters *a* to *i* indicate the displacement intervals adopted to analyse the evolution of the seismic *b* value and the fractal dimension *D* in Sections 5.3 and 5.4, respectively. The platen displacement, δ_a, was used in lieu of the axial strain, ε_a, because of the potential error that can be introduced into the AE count by duplicate values from the post-peak region, where the axial strain decreases.

Figure 12. (a) Spatial distribution of minerals in the UCS sample. Feldspar, quartz and biotite are indicated in grey, blue and green, respectively. (b–f) Cumulative spatial distribution of broken crack elements at increasing platen displacement values, δ_a, during the UCS test simulation: (b) $\delta_a = 0.25$ mm (stages *a* and *b*), (c) $\delta_a = 0.30$ mm (stages *a* to *d*), (d) $\delta_a = 0.35$ mm (stages *a* to *f*), (e) $\delta_a = 0.375$ mm (stages *a* to *h*), (f) $\delta_a = 0.425$ mm (stages *a* to *i*). Mode I (i.e. tensile) and mode II (i.e. shear) failures are indicated in orange and blue, respectively. A transition from diffuse-like tensile-dominated cracking to macroscopic spalling is captured as the sample is compressed.
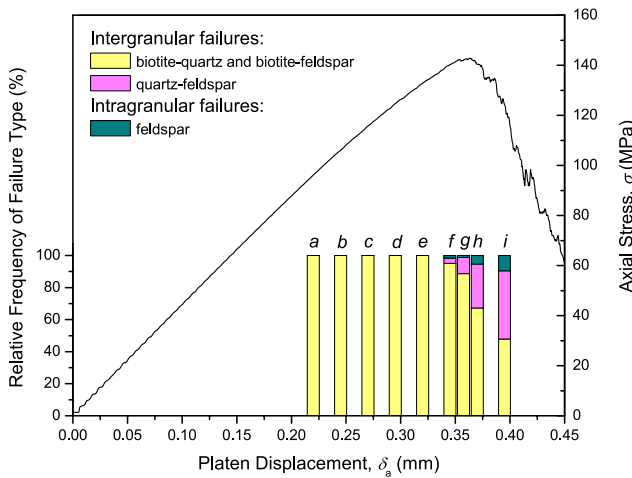
Figure 13. Relative frequency of failure types during the UCS test simulation. Intergranular failures correspond to the breakage of crack elements bonding together triangular elements representing different mineral phases, whereas intragranular failures correspond to the breakage of crack elements within the same mineral.

magnitude and frequency. Qualitatively, a similar loss of linearity for increasing applied stress was observed by Rao & Lakshmi (2005) during laboratory uniaxial compression tests on Godhra Granite.

The seismic *b* values during the UCS simulation, ranging between 0.76 and 1.80 (Fig. 15), are in good agreement with published experimental values for granitic rocks ranging between 1.1 and 2.4 (e.g. Lockner *et al.* 1991; Lockner 1993). The numerical results indicate two sharp drops in *b* value during the fracture process of the rock sample. The first drop occurs in the pre-peak region at about 75 per cent of the failure stress (stage *b*) and is characterized by a decrease from 1.80 to 0.99. As further discussed in Section 5.4, this unexpected variation is caused by few larger magnitude events clustering close to the bottom left corner of the sample which produce an increase in the share of large events for stage *b*. This localization of failure, which can be attributed to the particular spatial distribution of material properties, contributes to the non-linear behaviour of the sample's lateral displacement while does not have any sensible effect on its axial deformation response. The second decrease in the *b* value begins at 97 per cent of the failure stress (stage *g*), with *b* dropping from 1.59 to 1.08, and continues in the immediate post-

peak. This variation of *b*, clearly associated with the macroscopic rupture of the sample, is in agreement with several experimental findings (Scholz 1968a; Cai *et al.* 1988; Main & Meredith 1989; Meredith *et al.* 1990; Lockner *et al.* 1991; Amitrano 2003), which indicate a systematic decrease in *b* with increasing stress during deformation of intact rock samples. As depicted in Fig. 12, the *b* value decrease in correspondence to the maximum stress marks the transition from diffuse crack nucleation to crack coalescence in a major fracture plane.

5.4 Spatial clustering of AE

The location of AE sources has been widely used to study the crack redistribution during the rock failure process and, consequently, to obtain information on the fracture mechanisms. In this work, the process of spatial clustering of AE source locations, depicted in Fig. 16, was quantitatively analysed using the correlation integral (Hirata *et al.* 1987):

$$C(R) = \frac{2N_R(r < R)}{N(N-1)}, \qquad (28)$$

where $N_R(r < R)$ is the number of AE source pairs separated by a distance *r* shorter than *R*, and *N* is the total number of sources analysed. If the source distribution has a fractal structure, the correlation integral $C(R)$ is proportional to R^D, where *D* is the fractal dimension of the distribution

$$C(R) \sim R^D. \qquad (29)$$

In two dimensions, $D = 2$ indicates complete randomness in the source location distribution, while lower values suggest the presence of clustering. However, note that *D* does not carry any information about the shape of the spatial distribution: for example, $D = 1.0$ can refer to either a distribution of aligned sources or to a strongly clustered distribution around a point. Hence, to obtain information on the characteristics of the localization, the aforementioned fractal analysis must be accompanied with a visual inspection of the actual source pattern.

For distance *R* less than 50 mm, which corresponds to the width of the sample, the plots of $C(R)$ against *R* (Fig. 17) follow a good linear trend, indicating the fractal structure of AE source location distribution. Event spatial clustering that can be observed in Fig. 16 for stages *b*, *g*, *h* and *i*, manifests itself in the form of a decrease of fractal dimension to values $1.1 \leq D \leq 1.4$ (Fig. 17). The diffuse
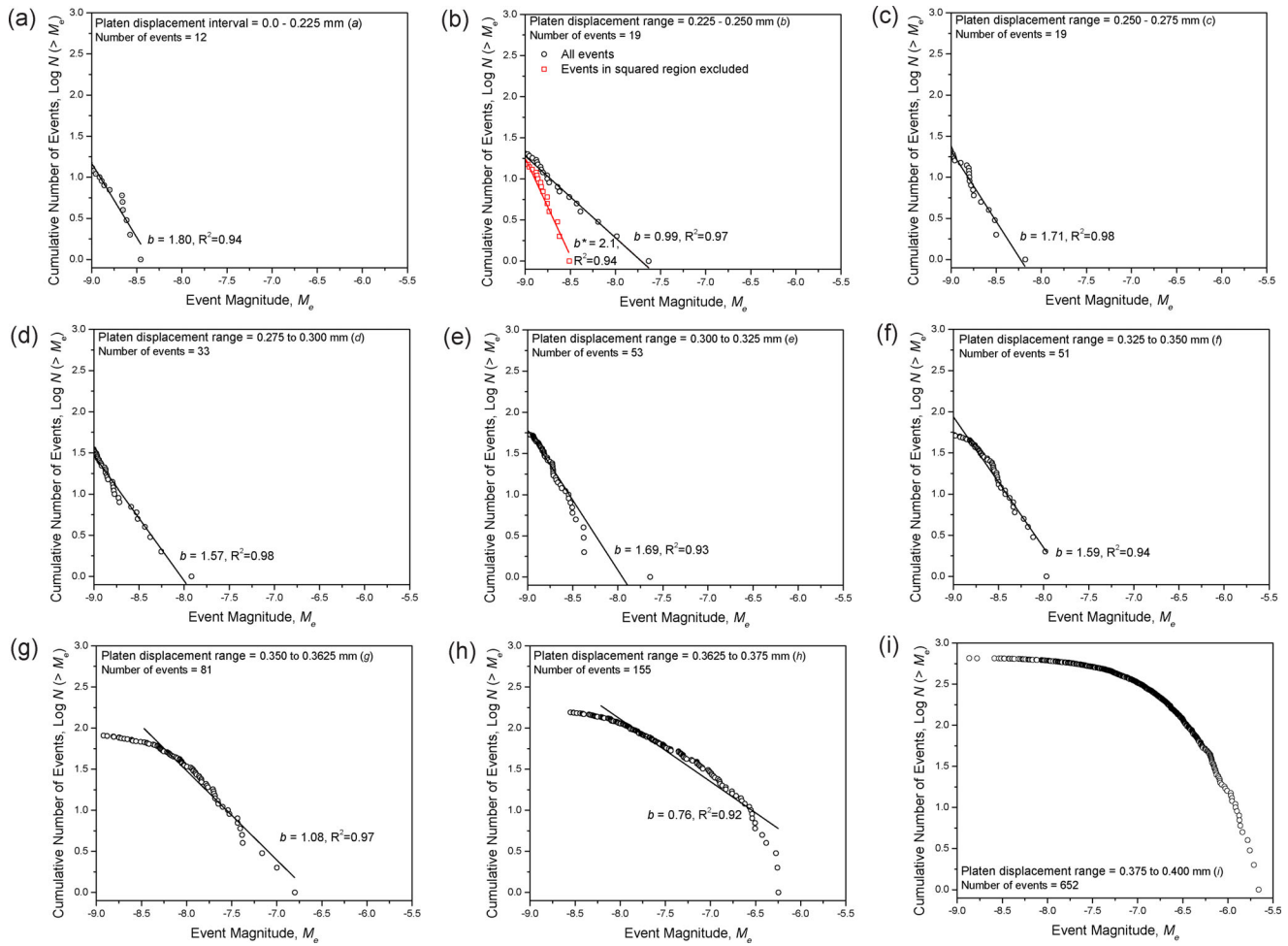
Figure 14. Frequency–magnitude plots for each displacement interval (stages *a* to *i*). Only events with magnitude $M_e \geq -9.0$ were considered. The exponent *b* was calculated for the linear part of each distribution together with the coefficient of determination, R^2, of the linear regression. Frequency–magnitude plots display a power-law distribution for axial displacement values less than the value at peak (stages *a* to *f*). In the peak and post-peak stages, the distributions lose linearity and a finite-size effect can be noted. The *b* value for stage *i* was not calculated. For stage *b*, an additional analysis was carried by excluding from the distribution the event cluster triggered by the bottom left corner of the sample (see Section 5.6).
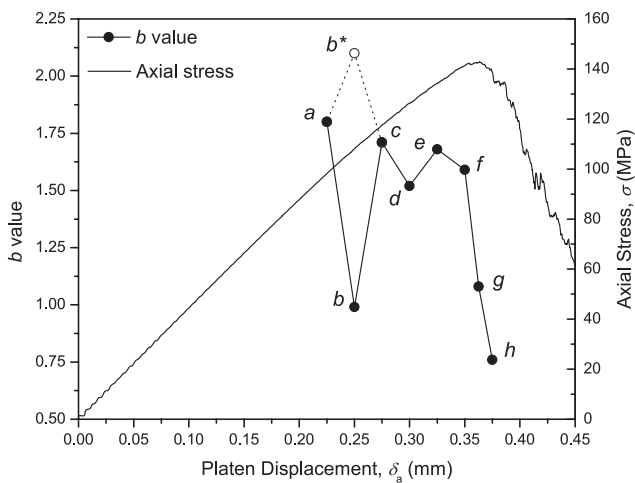

Figure 15. Variation of *b* value during the UCS test simulation. Drops in *b* value are associated with clustering of higher magnitude events due to either a localized effect (stage *b*) or to crack coalescence in a macroscopic rupture plane (stages *g* to *i*). For stage *b*, $b^* = 2.1$ was calculated by excluding from the distribution the cluster of events by the bottom left corner of the sample (see Section 5.6).

character of the damage pattern characterizing the other stages (*a*, *c* to *f*) is reflected in $1.4 \leq D \leq 1.8$. Due to the bidimensionality of the FEM/DEM model, the absolute values of fractal dimension could not be directly compared to experimental values, which vary in three dimensions between 0 and 3. Nevertheless, the simulated reduction of *D* before and after localization is in agreement with the laboratory results reported by Lockner (1993) and Shah & Labuz (1995) for compression tests on Westerly Granite and Charcoal Granite, respectively, and with other numerical simulations (e.g. Amitrano *et al.* 1999).

Finally, a comparison between the evolution of *b* value (Fig. 15) and fractal dimension *D* (Fig. 18) clearly shows a decrease of *b* value contemporary to the spatial localization of AE events, represented by a decrease of *D*, as observed by Lockner (1993). Higher *b* values result from low energy emission due to new crack formation and slow crack growth (i.e. diffuse damage), while lower *b* values are due to crack coalescence resulting in faster fracture growth accompanied by high energy emission.

5.5 Time evolution of AE rate

The stochastic self-similarity of the simulated microfracturing process was verified for the frequency–magnitude distribution
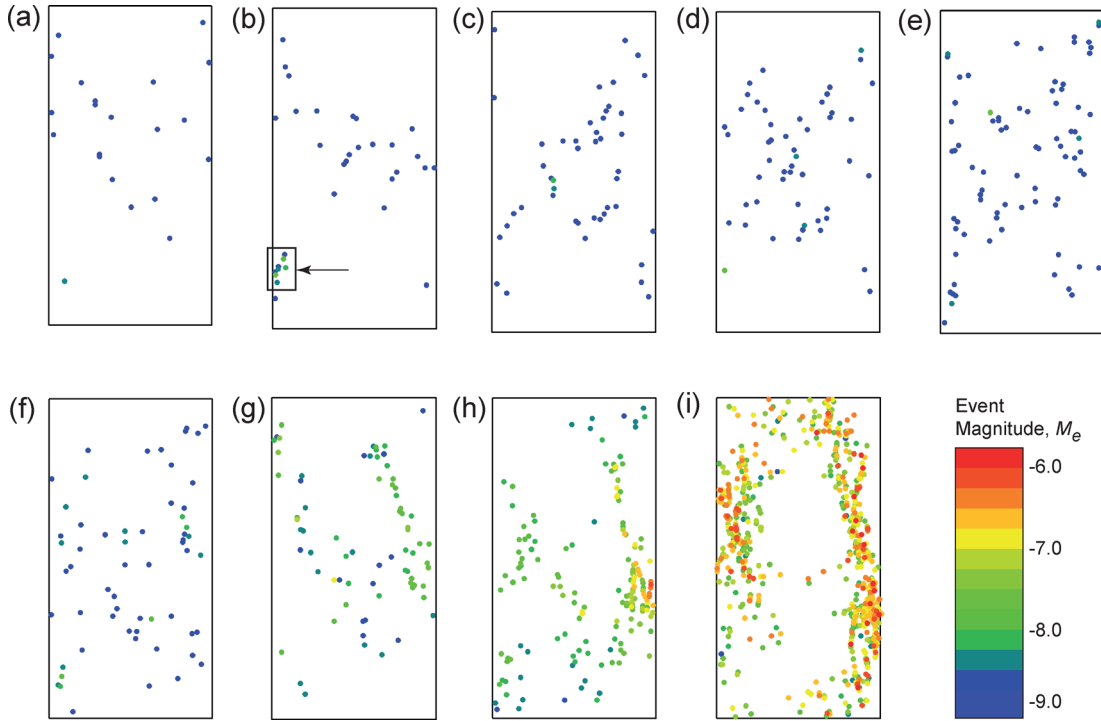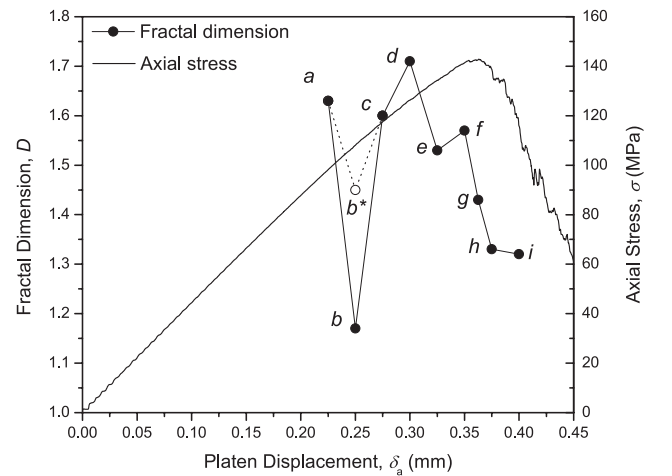
Figure 16. AE source locations and associated magnitude for stages *a* to *i* of the simulated UCS failure process. The colour bar indicates the event seismic magnitude, M_e, calculated from the kinetic energy of the sources using the technique illustrated in Section 4.2. Several events, with magnitude comprised between -8.5 and -7.5, cluster by the sample bottom left corner during stage *b* (indicated by an arrow), causing a drop in the correspondent *b* value and fractal dimension *D* (see Section 5.6). The macrorupture of the sample (stages *g* to *i*) is accompanied by the localization of high-energy events close to the sample lateral free surfaces in the form of spalls, as highlighted also by the fracture pattern depicted in Fig. 12(f).
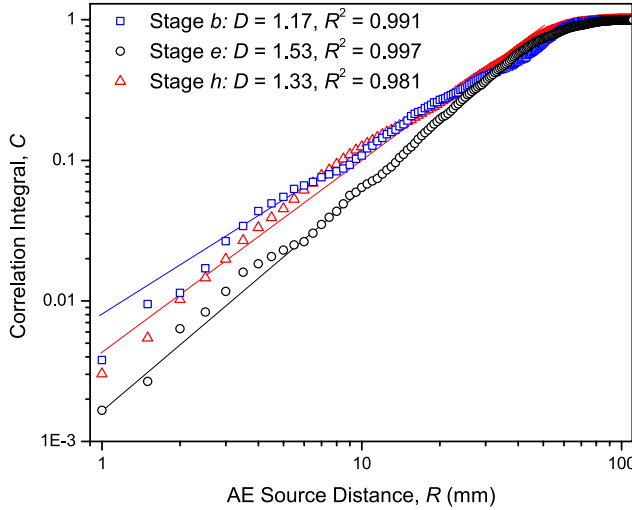
Figure 17. Correlation integral, $C(R)$, versus source distance, R, for stages *b*, *e* and *h* of the simulated UCS stress-displacement curve (Fig. 11). A linear regression is applied to the linear descending branch of each distribution ($R < 50$ mm) with slope equal to the fractal dimension *D*. The coefficient of determination, R^2, is also indicated.

Figure 18. Variation of fractal dimension *D* of the source location distribution during the UCS test simulation. Decrease of *D* value for stage *b* is caused by the local clustering of events indicated by the arrow in Fig. 16(b), whereas the decrease occurring in correspondence of the peak stress (stages *g* to *i*) is due to crack coalescence into macroscopic fractures. For stage *b*, $D^* = 1.45$ was calculated by excluding from the analysis the cluster of events by the bottom left corner of the sample (see Section 5.6).

(Section 5.3) and spatial distribution of AE sources (Section 5.4). As described earlier, this self-similarity manifests itself as the power laws expressed by eqs (26) and (29) in the magnitude and spatial domain, respectively. Similarly, it has been shown that also the rate of AE during rock fracture experiments follows a power-law evolution in the time domain (e.g. Scholz 1968b; Hirata 1987). This phenomenon is typically described by the Omori's law, an experimental relationship first introduced to characterize the rate of occurrence

of earthquake aftershocks (Omori 1894). In its generalized form, the Omori's law is expressed as (Utsu 1962)

$$\frac{\mathrm{d}N}{\mathrm{d}t} = \frac{K}{(c+t)^p}, \tag{30}$$

where $\mathrm{d}N/\mathrm{d}t$ is the aftershock rate, *t* is the time after the main shock and *K*, *c* and *p* are empirical fitting parameters. In the case

of foreshocks preceding the main rupture, t represents the reverse time from the main shock. In this numerical study, the temporal evolution of the simulated AE triggering was therefore studied with reference to the empirical description provided by eq. (30). As described in the following, both aftershocks and foreshocks were initially considered.

During laboratory experiments, a hyperbolic decay of the microfracturing activity with time is commonly recorded after the brittle fracture of rock sample with Omori's exponent p values typically ranging between 0.8 and 2.3 (Hirata 1987). This creep process produced by time-dependent fracturing mechanisms can be followed by AE monitoring provided that the rock sample remains intact (Scholz 1968b). For example, manual unloading at the onset of dynamic fracture can be performed to save the sample from excessive damage (Lei *et al.* 2004). In the FEM/DEM simulation, the analysis of aftershock sequences was heavily compromised by the model boundary conditions as well as the brittle behaviour exhibited by the sample under unconfined compression. Since the sample was loaded by means of platens moving at steady speed, a constant strain rate was applied for the entire duration of the simulation. Following the unstable rupture of the sample, this monotonic loading condition greatly enhanced the fragmentation of the rock, thus causing a dramatic increase of breakages in the post-peak stages of the simulation (Fig. 11). That is, the simulation was stopped before any decay in the event rate could be observed.

Conversely, acoustic events triggered before the macroscopic failure of the sample could be successfully analysed. The evolution of AE rate as function of the time prior to the main rupture is reported in the logarithmic scale plot of Fig. 19. For time values t greater than 0.9 ms (i.e. stage a in Fig. 11), very low activity is recorded and the evolution is non-linear. However, as more stress is applied, more events are triggered and a slow growth of microfracturing is followed by a rapid acceleration of AE rate, for which Omori's law provides a good fit. Due to the above-mentioned difficulties, a clear identification of the time, t_M, corresponding to the main shock was not possible. Therefore, the regression analysis using Omori's law was repeated for three increasing t_M values: p values equal to 0.38,

Figure 19. Logarithmic scale plot of the rate of acoustic events in the UCS test simulation as function of the time before the main rupture. Omori's exponent values, p (eq. 30), equal to 0.38, 0.70 and 1.12 were calculated by assuming the main rupture to occurred at axial displacement values, δ_a, of 0.3625, 0.375 and 0.400 mm, respectively. These threshold displacement values to the endpoints of stages g, h and i, respectively (Fig. 11).

0.70 and 1.12 were obtained for t_M equal to 1.45, 1.50 and 1.60 ms, respectively. Given a platen velocity of $v = 0.125\,\mathrm{m\,s^{-1}}$, these t_M values correspond to axial displacements, δ_a, of 0.3625, 0.375 and 0.400 mm, which in turn correspond to the endpoints of stages g, h and i, respectively. For comparison, p values ranging between 0.8 and 2.1 have been reported for foreshocks during actual laboratory tests on rock (e.g. Ojala *et al.* 2004; Schubnel *et al.* 2007).
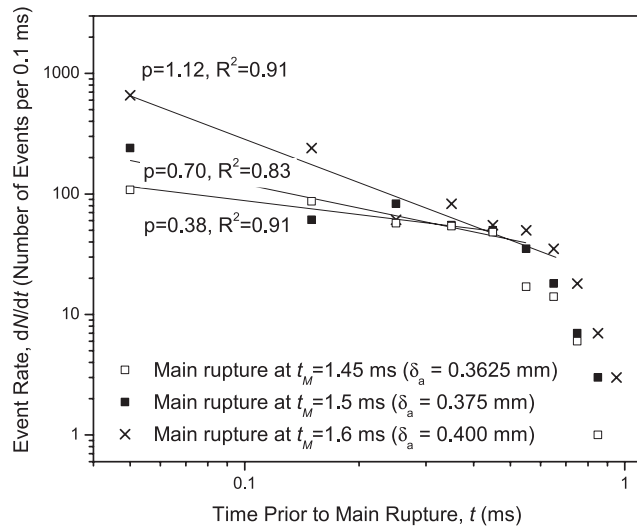
5.6 Analysis of b value anomaly

As described in Section 5.3, an anomaly of b value was recorded during stage b ($0.225 \leq \delta_a \leq 0.250$ mm) of the UCS test simulation. The b value, calculated from the frequency–magnitude distribution of all events in the given displacement window, was equal to 0.99, which represented a 40 per cent reduction with respect to the average value in the pre-peak stages of the simulation ($b = 1.67$, Fig. 15). Moreover, the drop in b value was also accompanied by a reduction in the associated fractal dimension, D, of the hypocentre distribution (Fig. 18).

For tectonic earthquakes, correlations between low b values and regions of increased fault strength have been observed (e.g. Wiemer & Wyss 1997). In the laboratory, temporal fluctuations of AE statistics have been related to the heterogeneous distribution of grain size and strength within the rock microstructure (Lei *et al.* 2004). For example, Goebel *et al.* (2012) showed a clear connection between the spatiotemporal distribution of microseismicity and structural heterogeneities of fracture surfaces during stick-slip laboratory experiments on notched samples of Westerly Granite. More specifically, geometric asperities identified through CT scan images corresponded well with regions of low local b value.
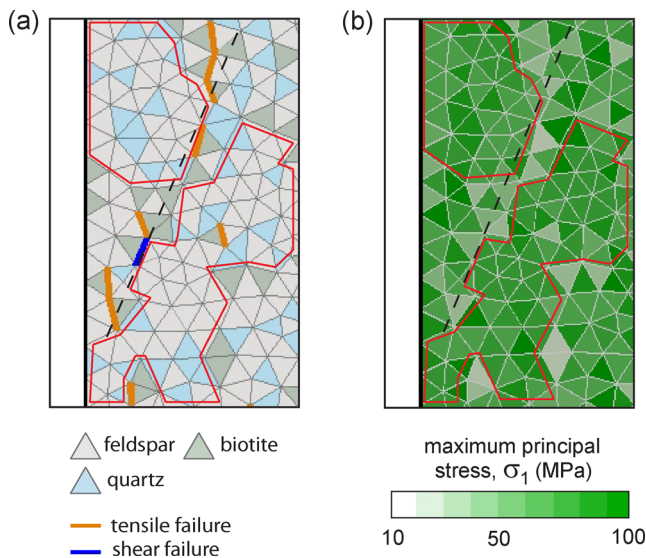
In the FEM/DEM simulation, a region of high event density was located during stage b in proximity to the bottom left corner of the sample (Fig. 16b). The effect of this cluster of events on the simulated AE statistics, namely b value and fractal dimension D, was assessed by excluding these events from the regression analysis based on eqs (27) and (29). The modified distributions of event magnitude (Fig. 14b) and spatial correlation integral were characterized by $b^* = 2.1$ and $D^* = 1.45$, respectively. As can be observed from Figs 15 and 18, these values tend to follow the same trend simulated for the other pre-peak stages, thus confirming the influence of the event sequence in causing the simulated anomaly.

The local distribution of mineral phases was then investigated in an attempt to provide a mechanical interpretation for the simulated phenomenon (Fig. 20a). The acoustic events correspond to the failure of a series of crack elements approximately aligned at about $67°$ from the horizontal. In agreement with the analysis reported in Section 5.2, breakages are mainly restricted to the weaker interfaces between biotite and feldspar in the form of mode I fracturing. The visual inspection of the property distribution indicates the presence of two quartz–feldspar clumps located on the top left and bottom right side of the rupture plane. These two mineral clumps, characterized by higher stiffness and strength values (Table 5), experience a concentration of maximum principal stress, σ_1 (Fig. 20b). As discussed in detail by Mahabadi (2012), breakage of weaker mineral interfaces is due to higher localized tensile stresses arising from elastic mismatch of the three rock minerals. Based on these observations, it is likely that the simulated higher activity is a direct consequence of the build-up of elastic strain energy in the two clumps which is released as acoustic energy upon failure of the weaker interfaces. Therefore, these numerical results tend to agree with the experimental evidence mentioned earlier which highlights decreasing b

Figure 20. A zoomed-in view of the squared region of Fig. 16(b) showing (a) the distribution of mineral phases and failed crack elements during stage *b* of the UCS test simulation and (b) the local distribution of maximum principal stress, σ_1, before the rupture sequence at $t = 0.68$ ms (i.e. $\delta_a = 0.17$ mm). The approximate alignment direction of the sequence of events is indicated by a dashed line. These events tend to be located at the interface of two clumps of stiffer, stronger material (i.e. feldspar and quartz) contoured by a red line. Note the heterogeneous stress distribution with two major compressive stress concentrations.

values due to fracture growth around the boundaries of asperities. Nevertheless, further numerical investigation is required to confirm the validity of the postulated mechanism. In this context, a more realistic numerical representation of the rock microstructure, for instance directly derived from μCT images (Mahabadi *et al.* 2012b), should be adopted.

6 SUMMARY

Monitoring of acoustic activity has been used to characterize the rock failure process by providing unique information regarding the amount of internal damage, the spatial distribution of microfractures and the magnitude distribution of fracturing events. Therefore, the ability to simulate acoustic activity presents an important tool in the validation of numerical models that aim at quantitatively capturing the deformation and failure process of brittle rocks. Furthermore, the relationship between the simulated seismicity and model parameters (e.g. material properties, loading conditions, degree of heterogeneity) can be numerically investigated. While several models have been developed to date for this purpose, only a limited number explicitly consider acoustic waves, the majority adopting a static approach, whereby the elastic strain energy, dissipated by an elastoplastic constitutive law, is considered as an equivalent for the radiated seismic energy.

In this work, a new approach to simulate the acoustic activity of brittle failing rocks was presented based on the combined FEM/DEM. Two methods were considered to obtain quantitative information on the acoustic activity: (i) the seismic analysis of waveforms recorded at a distance from the sources and (ii) monitoring of internal variables (e.g. relative displacements and kinetic energy) in proximity to propagating fractures.

Fourier analysis of synthetic seismograms highlighted frequency contents ranging between 8 and 20 kHz. As expected, the amount

of applied numerical damping significantly reduced the amplitudes of AE signals recorded at a distance from the source. Low rupture speed values, direct consequence of the adopted mesoscopic model of the fracturing process, resulted in a quasi-dynamic AE behaviour characterized by low-frequency content source processes in the FEM/DEM simulations. Although seismic energy is emitted upon failure, the observed low rupture speeds imply that most released energy is dissipated as fracture energy within the FPZ. Furthermore, the seismic analysis of synthetic seismograms suffered from the inability to record temporally distinct events as the event count rate increases, which constrained its application to special fracturing conditions (e.g. wing crack propagation). Nevertheless, event relocation based on traveltime inversion showed good agreement with the internally recorded AE locations. Also, the seismic energy estimated at the receivers via integration of wave amplitude scaled linearly with the kinetic energy of cracks monitored at the source.

Taking advantage of the discrete material representation of FEM/DEM, an alternative algorithm was implemented to obtain seismic information, including source location, mode of fracture, initiation time and event energy, based on internal monitoring of node motions. As mentioned earlier, the event energy, estimated based on the crack kinetic energy, was related to the energy carried by the radiated stress waves and recorded at selected locations by the model boundaries. The main limitation of this technique is represented, at the moment, by its inability to record the energy radiated by slips along pre-existing crack surfaces that do not involve intact material breakage. Finally, the validity of the aforementioned approach was demonstrated by simulating the AE of an unconfined compression test on Stanstead Granite. The model reproduced the macroscopic mechanical response of the sample (e.g. elastic behaviour, overall strength, post-peak brittle failure), as observed in the laboratory. Simulated event magnitudes tended to display a power-law distribution, with *b* values in agreement with those reported in the literature for granitic rocks. Also, the model showed a correlation between the decrease of *b* value and the transition of source location distribution from diffuse-like to strongly clustered, as the applied stress increases and macroscopic fractures develop through the sample. A *b* value anomaly was related to the failure of weaker mineral bonds at the interface of stronger, stiffer clumps within the numerical microstructure of the rock sample. Furthermore, Omori's law provided a good fit for the evolution of AE rate as function of time before the macroscopic rupture of the sample.

In future studies, the validated FEM/DEM-AE modelling technique will be used to obtain further insights into the micromechanics of rock failure with potential applications ranging from laboratory-scale microcracking to engineering-scale processes (e.g. underground excavations, petroleum and geothermal reservoirs) to tectonic earthquakes. Moreover, the approach will be extended to a 3-D version of the FEM/DEM code currently under development.

ACKNOWLEDGEMENTS

to thank Dr Alexandre Schubnel and one anonymous reviewer for their valuable comments and suggestions to improve the quality of the paper.

REFERENCES

Alava, M.J., Nukala, P.K.V.V. & Zapperi, S., 2006. Statistical models of fracture, *Adv. Phys.,* **55**(3–4), 349–476.

Amitrano, D., 2003. Brittle-ductile transition and associated seismicity: experimental and numerical studies and relationship with the *b* value, *J. geophys. Res.,* **108**(B1), 2044, doi:10.1029/2001JB000680.

Amitrano, D., Grasso, J.-R. & Hantz, D., 1999. From diffuse to localised damage through elastic interaction, *Geophys. Res. Lett.,* **26**(14), 2109–2112.

Andreykiv, O.Y., Lysak, M.V., Serhiyenko, O.M. & Skalsky, V.R., 2001. Analysis of acoustic emission caused by internal cracks, *Eng. Fract. Mech.,* **68**(11), 1317–1333.

Barenblatt, G., 1962. The mathematical theory of equilibrium cracks in brittle fracture, *Adv. appl. Mech.,* **7**(C), 55–129.

Benson, P.M., Vinciguerra, S., Meredith, P.G. & Young, R.P., 2008. Laboratory simulation of volcano seismicity, *Science,* **322**(5899), 249–252.

Bizzarri, A., 2011. On the deterministic description of earthquakes, *Rev. Geophys.,* **49**, RG3002, doi:10.1029/2011RG000356.

Brace, W. & Bombolakis, E., 1963. A note on brittle crack growth in compression, *J. geophys. Res.,* **68**(12), 3709–3713.

Cai, D., Fang, Y., Zhang, W.S.L., Li, J. & Geng, N., 1988. The b-value of acoustic emission during the complete process of rock fracture, *Acta Seismol. Sin.,* **2**, 129–134.

Carpinteri, A. & Bocca, P., 1991. *Damage and Diagnosis of Materials and Structures,* Pitagora Editrice, Bologna.

Cotterell, B. & Rice, J., 1980. Slightly curved or kinked cracks, *Int. J. Fract.,* **16**(2), 155–169.

Cundall, P.A. & Hart, R.D., 1992. Numerical modelling of discontinua, *Eng. Comput.,* **9**(2), 101–113.

Dugdale, D., 1960. Yielding of steel sheets containing slits, *J. Mech. Phys. Solids,* **8**(2), 100–104.

Eberhardt, E., Stead, D., Stimpson, B. & Read, R., 1997. Changes in acoustic event properties with progressive fracture damage, *Int. J. Rock Mech. Min. Sci.,* **34**(3-4), paper no. 071B.

Evans, R. & Marathe, M., 1968. Microcracking and stress-strain curves for concrete in tension, *Mater. Struct.,* **1**(1), 61–64.

Falls, S.D. & Young, R.P., 1998. Acoustic emission and ultrasonic-velocity methods used to characterize the excavation disturbance associated with deep tunnels in hard rock, *Tectonophysics,* **289**(1–3), 1–15.

Fang, Z. & Harrison, J.P., 2002. Application of a local degradation model to the analysis of brittle fracture of laboratory scale rock specimens under triaxial conditions, *Int. J. Rock Mech. Min. Sci.,* **39**(4), 459–476.

Feng, X.T., Pan, P.Z. & Zhou, H., 2006. Simulation of the rock microfracturing process under uniaxial compression using an elasto-plastic cellular automaton, *Int. J. Rock Mech. Min. Sci.,* **43**(7), 1091–1108.

Freund, L.B., 1972. Energy flux into the tip of an extending crack in an elastic solid, *J. Elast.,* **2**(4), 341–349.

Freund, L.B., 1990. *Dynamic Fracture Mechanics,* Cambridge University Press, Cambridge.

Goebel, T.H.W., Becker, T.W., Schorlemmer, D., Stanchits, S., Sammis, C., Rybacki, E. & Dresen, G., 2012. Identifying fault heterogeneity through mapping spatial anomalies in acoustic emission statistics, *J. geophys. Res.,* **117**, 1–18.

Gutenberg, B., 1956. The energy of earthquakes, *Q. J. geol. Soc.,* **112**, 1–14.

Hanks, T.C., 1992. Small earthquakes, tectonic forces, *Science,* **256**(5062), 1430–1432.

Hazzard, J. & Young, R., 2000. Simulating acoustic emissions in bonded-particle models of rock, *Int. J. Rock Mech. Min. Sci.,* **37**(5), 867–872.

Hazzard, J. & Young, R., 2004. Dynamic modelling of induced seismicity, *Int. J. Rock Mech. Min. Sci.,* **41**(8), 1365–1376.

Hazzard, J., Collins, D., Pettitt, W. & Young, R., 2002. Simulation of unstable fault slip in granite using a bonded-particle model, *Pure appl. Geophys.,* **159**(1–3), 221–245.

Hazzard, J.F. & Young, R., 2002. Moment tensors and micromechanical models, *Tectonophysics,* **356**(1–3), 181–197.

Hillerborg, A., Modeer, M. & Petersson, P.-E., 1976. Analysis of crack formation and crack growth in concrete by means of fracture mechanics and finite elements, *Cement Concr. Res.,* **6**(6), 773–781.

Hirata, T., 1987. Omori's power law aftershock sequence of microfracturing in rock fracture experiment, *J. geophys. Res.,* **92**(B7), 6215–6221.

Hirata, T., Satoh, T. & Ito, K., 1987. Fractal structure of spatial distribution of microfracturing in rock, *Geophys. J. R. astr. Soc.,* **90**(2), 369–374.

Hirose, S. & Achenbach, J., 1991. Acoustic emission and near-tip elastodynamic fields of a growing penny-shaped crack, *Eng. Fract. Mech.,* **39**(1), 21–36.

Hjörleifsdóttir, V., 2007. Earthquake source characterization using 3D numerical modeling, *PhD thesis,* Caltech.

Hoek, E. & Bieniawski, Z., 1965. Brittle failure propagation in rock compression, *Int. J. Fract. Mech.,* **1,** 137–155.

Holcomb, D.J., Stone, C.M. & Costin, L.S., 1990. Combining acoustic emission locations and a microcrack damage model to study development of damage in brittle materials, in *Proceedings of the 31st U.S. Symposium on Rock Mechanics (USRMS),* Golden, CO, pp. 645–651.

Horii, H. & Nemat-Nasser, S., 1986. Brittle failure in compression: splitting, faulting, and brittle-ductile transition, *Phil. Trans. R. Soc. Lond.,* **319**(1549), 337–374.

House, L., 1987. Locating microearthquakes induced by hydraulic fracturing in crystalline rock, *Geophys. Res. Lett.,* **14**(9), 919–921.

Ida, Y., 1972. Cohesive force across the tip of a longitudinal-shear crack and Griffith's specific surface energy, *J. geophys. Res.,* **77**(20), 3796–3805.

Invernizzi, S., Carpinteri, A., Lacidogna, G. & Manuello, A., 2011. Numerical simulation of AE activity in quasi-brittle materials under compression, in *Experimental Mechanics on Emerging Energy Systems and Materials, Volume 5, vol. 16 of Conference Proceedings of the Society for Experimental Mechanics Series,* pp. 109–116, ed. Proulx, T., Springer, New York.

Irwin, G., 1957. Analysis of stresses and strains near the end of a crack traversing a plate, *J. appl. Mech.,* **24,** 361–364.

Ishii, M., Shearer, P.M., Houston, H. & Vidale, J.E., 2005. Extent, duration and speed of the 2004 Sumatra-Andaman earthquake imaged by the Hi-Net array, *Nature,* **435**(7044), 933–936.

Kanamori, H. & Brodsky, E.E., 2004. The physics of earthquakes, *Rep. Prog. Phys.,* **67,** 1429–1496.

Labuz, J.F., Shah, S.P. & Dowding, C.H., 1985. Experimental analysis of crack propagation in granite, *Int. J. Rock Mech. Min. Sci. Geomech. Abstr.,* **22**(2), 85–98.

Lawn, B., 1993. *Fracture of Brittle Solids,* Cambridge University Press, Cambridge.

Lehner, F. & Kachanov, M., 1996. On modelling of winged cracks forming under compression, *Int. J. Fract.,* **77**(4), R69–R75.

Lei, X., Masuda, K., Nishizawa, O., Jouniaux, L., Liu, L., Ma, W., Satoh, T. & Kusunose, K., 2004. Detailed analysis of acoustic emission activity during catastrophic fracture of faults in rock, *J. Struct. Geol.,* **26,** 247–258.

Lockner, D., 1993. The role of acoustic emission in the study of rock fracture, *Int. J. Rock Mech. Min. Sci. Geomech. Abstr.,* **30**(7), 883–899.

Lockner, D.A., Byerlee, J.D.B., Kusenko, V., Ponomarev, A. & Sidorin, A., 1991. Quasi-static fault growth and shear fracture energy in granite, *Nature,* **350**(6313), 39–42.

Lyakhovsky, V., Ben-Zion, Y. & Agnon, A., 1997. Distributed damage, faulting, and friction, *J. geophys. Res.,* **102**(B12), 27 635–27 649.

Lyakhovsky, V., Ben-Zion, Y. & Agnon, A., 2001. Earthquake cycle, fault zones, and seismicity patterns in a rheologically layered lithosphere, *J. geophys. Res.,* **106**(B3), 4103–4120.

Lysak, M., 1996. Development of the theory of acoustic emission by propagating cracks in terms of fracture mechanics, *Eng. Fract. Mech.,* **55**(3), 443–452.

Mahabadi, O.K., 2012. Investigating the influence of micro-scale heterogeneity and microstructure on the failure and mechanical behaviour of geomaterials, *PhD thesis,* Department of Civil Engineering, University of Toronto, Canada.

Mahabadi, O.K., Cottrell, B.E. & Grasselli, G., 2010a. An example of realistic modelling of rock dynamics problems: FEM/DEM simulation of dynamic Brazilian test on Barre granite, *Rock Mech. Rock Eng.,* **43**(6), 707–716.

Mahabadi, O.K., Grasselli, G. & Munjiza, A., 2010b. Y-GUI: a graphical user interface and pre-processor for the combined finite-discrete element code, Y2D, incorporating material inhomogeneity, *Comput. Geosci.,* **36**(2), 241–252.

Mahabadi, O.K., Lisjak, A., Grasselli, G. & Munjiza, A., 2012a. Y-Geo: a new combined finite-discrete element numerical code for geomechanical applications, *Int. J. Geomech.,* **12**(6), 676–688.

Mahabadi, O.K., Randall, N.X., Zong, Z. & Grasselli, G., 2012b. A novel approach for micro-mechanical characterization and modelling of geomaterials incorporating actual material heterogeneity, *Geophys. Res. Lett.,* **39**, L01303, doi:10.1029/2011GL050411.

Main, I.G. & Meredith, P.G., 1989. Classification of earthquake precursors from a fracture mechanics model, *Tectonophysics,* **167**(2–4), 273–283.

Majer, E.L. & Doe, T.W., 1986. Studying hydrofractures by high frequency seismic monitoring, *Int. J. Rock Mech. Min. Sci. Geomech. Abstr.,* **23**(3), 185–199.

Mavko, G., Mukerji, T. & Dvorkin, J., 2009. *The Rock Physics Handbook: Tools for Seismic Analysis of Porous Media,* 2nd edn, Cambridge University Press, New York.

Meredith, P.G., Main, I.G. & Jones, C., 1990. Temporal variations in seismicity during quasi-static and dynamic rock failure, *Tectonophysics,* **175**(1–3), 249–268.

Minozzi, M., Caldarelli, G., Pietronero, L. & Zapperi, S., 2003. Dynamic fracture model for acoustic emission, *Eur. Phys. J. B,* **36**(2), 203–207.

Mogi, K., 1962. Magnitude frequency relations for elastic shocks accompanying fractures of various materials and some related problems in earthquakes, *Bull. Earthq. Res. Inst. Univ. Tokyo,* **40**(4), 831–853.

Mogi, K., 1967. Earthquakes and fractures, *Tectonophysics,* **5**(1), 35–55.

Munjiza, A., 2004. *The Combined Finite-Discrete Element Method,* John Wiley & Sons Ltd, Chichester, West Sussex, England.

Munjiza, A. & Andrews, K.R.F., 2000. Discretised penalty function method in combined finite-discrete element analysis, *Int. J. Numer. Methods Eng.,* **49**(11), 1495–1520.

Munjiza, A., Owen, D.R.J. & Bicanic, N., 1995. A combined finite-discrete element method in transient dynamics of fracturing solids, *Eng. Comput.,* **12**(2), 145–174.

Munjiza, A., Andrews, K.R.F. & White, J.K., 1999. Combined single and smeared crack model in combined finite-discrete element analysis, *Int. J. Numer. Methods Eng.,* **44**(1), 41–57.

Nemat-Nasser, S. & Horii, H., 1982. Compression-induced nonplanar crack extension in with application to splitting, exfoliation, and rockburst, *J. geophys. Res.,* **87**, 6805–6821.

Obert, L. & Duvall, W., 1957. Micro-seismic method of determining the stability of underground openings, Technical report, U.S. Bureau of Mines.

Ojala, I.O., Main, I.G. & Ngwenya, B.T., 2004. Strain rate and temperature dependence of Omori law scaling constants of AE data: implications for earthquake foreshock-aftershock sequences, *Geophys. Res. Lett.,* **31**, L24617, doi:10.1029/2004GL020781.

Omori, F., 1894. On the aftershocks of earthquakes, *J. Coll. Sci. Imperial Univ. Tokyo,* **7**, 111–120.

Pearson, C., 1981. The relationship between microseismicity and high pore pressures during hydraulic stimulation experiments in low permeability granitic rocks, *J. geophys. Res.,* **86**(B9), 7855–7864.

Pettitt, S., Baker, C., Young, R., Dahlström, L.-O. & Ramqvist, G., 2002. The assessment of damage around critical engineering structures using induced seismicity and ultrasonic techniques, *Pure appl. Geophys.,* **159**(1–3), 179–195.

Potyondy, D.O. & Cundall, P.A., 2004. A bonded-particle model for rock, *Int. J. Rock Mech. Min. Sci.,* **41**(8), 1329–1364.

Rao, M.V.M.S. & Lakshmi, K.J.P., 2005. Analysis of b-value and improved b-value of acoustic emissions accompanying rock fracture, *Curr. Sci.,* **89**(9), 1577–1582.

Richter, C., 1958. *Elementary Seismology,* W.H. Freeman, San Francisco.

Scholz, C.H., 1968a. The frequency magnitude relation of microfracturing in rock and its relationship to earthquakes, *Bull. seism. Soc. Am.,* **58**(1), 399–415.

Scholz, C.H., 1968b. Microfractures, aftershocks, and seismicity, *Bull. seism. Soc. Am.,* **58**, 1117–1130.

Schubnel, A., Thompson, B.D., Fortin, J., Guéguen, Y. & Young, R.P., 2007. Fluid-induced rupture experiment on Fontainebleau sandstone: premonitory activity, rupture propagation, and aftershocks, *Geophys. Res. Lett.,* **34**, L19307, doi:10.1029/2007GL031076.

Shah, K.R. & Labuz, J.F., 1995. Damage mechanics in stressed rock from acoustic emission, *J. geophys. Res.,* **100**(B8), 15 527–15 539.

Tang, C., 1997. Numerical simulation of progressive rock failure and associated seismicity, *Int. J. Rock Mech. Min. Sci.,* **34**(2), 249–261.

Tang, C.A. & Kaiser, P.K., 1998. Numerical simulation of cumulative damage and seismic energy release during brittle rock failure—part I: fundamentals, *Int. J. Rock Mech. Min. Sci.,* **35**(2), 113–121.

Tang, C.A., Chen, Z.H., Xu, X.H. & Li, C., 1997. A theoretical model for Kaiser effect in rock, *Pure appl. Geophys.,* **150**(2), 203–215.

Thompson, B., Young, R. & Lockner, D., 2006. Fracture in Westerly Granite under AE feedback and constant strain rate loading: nucleation, quasi-static propagation, and the transition to unstable fracture propagation, *Pure appl. Geophys.,* **163**(5–6), 995–1019.

Utsu, T., 1962. On the nature of three Alaskan aftershocks sequences of 1957 and 1958, *Bull. seism. Soc. Am.,* **52**, 279–297.

Wang, Y.C., Yin, X.C., Ke, F.J. & Xia, M.F., 2000. Numerical simulation of rock failure and earthquake process on mesoscopic scale, *Pure appl. Geophys.,* **157**(11–12), 1905–1928.

Wiemer, S. & Wyss, M., 1997. Mapping the frequency-magnitude distribution in asperities: an improved technique to calculate recurrence times? *J. geophys. Res.,* **102**(B7), 11 115–15 128.

Young, R.P. & Maxwell, S.C., 1992. Seismic characterization of a highly stressed rock mass using tomographic imaging and induced seismicity, *J. geophys. Res.,* **97**(B9), 361–373.

Yuan, S. & Harrison, J., 2006. A review of the state of the art in modelling progressive mechanical breakdown and associated fluid flow in intact heterogeneous rocks, *Int. J Rock Mech. Min. Sci.,* **43**(7), 1001–1022.

Zaitsev, Y.V., 1985. *Mechanics of Geomaterials: Rocks, Concretes, Soils,* chap. 6, pp. 89–128, John Wiley & Sons Ltd, Evanston, IL.

Zapperi, S., Vespignani, A. & Stanley, H.E., 1997. Plasticity and avalanche behaviour in microfracturing phenomena, *Nature,* **388**(6643), 658–660.

Zhu, W., Zhao, X., Kang, Y., Wei, C. & Tian, J., 2010. Numerical simulation on the acoustic emission activities of concrete, *Mater. Struct.,* **43**(5), 633–650.

Zietlow, W. & Labuz, J., 1998. Measurement of the intrinsic process zone in rock using acoustic emission, *Int. J. Rock Mech. Min. Sci.,* **35**(3), 291–299.